Journal of the European Ceramic Society 45 (2025) 116875

Contents lists available at ScienceDirect

Journal of the European Ceramic Society

journal homepage: www.elsevier.com/locate/jeurceramsoc

Original article

Multiphase-field modeling of domain structure evolution in ferroelectric thin film

Ling Fan [a,*], Martin Reder [a,b], Daniel Schneider [b,c], Manuel Hinterstein [d], Britta Nestler [a,b,c]

[a] Institute for Applied Materials (IAM), Karlsruhe Institute of Technology, Karlsruhe, 76131, Germany
[b] Institute of Digital Materials Science (IDM), Karlsruhe University of Applied Sciences, Karlsruhe, 76133, Germany
[c] Institute of Nanotechnology (INT), Karlsruhe Institute of Technology, Karlsruhe, 76131, Germany
[d] Fraunhofer Institute for Mechanics of Materials, Freiburg, 79108, Germany

ARTICLE INFO

Keywords:
Multiphase-field method
Ferroelectric thin film
Domain structure

ABSTRACT

The computational determination of domain structures in ferroelectric films is achieved through the implementation of a multiphase-field methodology. In this framework, domain structures are calculated by minimizing the total energy functional with respect to the multiphase-field order parameter $\boldsymbol{\phi}$. This energy functional includes the general interfacial energy, which consists of a multi-obstacle potential and a gradient energy, as well as the phase-dependent bulk energy that incorporates contributions from mechanical forces and electric fields. Using $PbTiO_3$ (PTO) as the chosen model material, we report on the results of investigating domain structures, including an examination of the influence of substrate deformation, variations in misfit strains, different thin film thicknesses, and temperature fluctuations. By implementing the mechanical jump condition approach, the inelastic strain is calculated independently for both the thin film and the substrate, under different conditions. Furthermore, this model demonstrates its ability to investigate domain structures without relying on the Landau potential to characterize the structural stability, providing a valuable reference for studing various ferroelectric thin films that lack higher-order Landau coefficients.

1. Introduction

Ferroelectric thin films exhibit remarkable properties due to their intrinsic electrical polarization, with thicknesses in the nanometer range. Their ability to switch their polarization in response to an electric field, together with their extraordinary piezoelectric, pyroelectric, and nonlinear optical properties, places them at the forefront of research and development in fields as diverse as sensors, memory devices, photovoltaic, and others [1–4]. Domain structures represent an inherent characteristic within ferroelectric thin films, which play a defining role in shaping their performance. A deep understanding of the domain structures, coupled with the manipulation of their configurations, is therefore of importance for developing the ferroelectric thin films.

Relying on the time-dependent Ginzburg–Landau theory (TDGL), the phase-field method has been successfully used to predict the domain structure and phase transformation for ferroelectric materials [5–11]. In particular, the methodology presented by Li et al. in Ref. [12] for investigating the mechanical boundary conditions of ferroelectric films constrained by a substrate has paved the way for extensive investigations of ferroelectric thin films, using the phase-field method. Over the past two decades, this approach has played an indispensable role in elucidating the intricacies of ferroelectric transformations and the resulting domain structures in a variety of ferroelectric thin films [8,10–13]. These investigations have covered a wide range of scenarios, including the effects of mechanical strain and electrical control, along with considerations related to thin film thickness and other relevant variables [8,14,15]. In addition to the inclusion of the strain gradient effect, the investigation of the flexoelectric properties of ferroelectric thin films has developed into an important field of research [16–18]. Furthermore, improvements in boundary conditions and the limitation of dimensional parameters enable the model to study nanostructures such as nanoislands [19], nanodots [20,21], nanowires [22,23], and super lattices [24,25].

It is important to recognize that the polarization vector is the order parameter in the TDGL model. Simultaneously, the domain structure serves as a result of energy minimization concerning polarization, encompassing the Landau potential, elastic, electrical, and domain wall energies. The stability of the polarization state depends on a thorough consideration of a higher-order Landau potential that includes terms

* Corresponding author.
E-mail addresses: ling.fan@kit.edu (L. Fan), martin.reder@kit.edu (M. Reder), daniel.schneider@kit.edu (D. Schneider), manuel.hinterstein@iwm.fraunhofer.de (M. Hinterstein), britta.nestler@kit.edu (B. Nestler).

https://doi.org/10.1016/j.jeurceramsoc.2024.116875
Received 9 April 2024; Received in revised form 7 August 2024; Accepted 26 August 2024
Available online 28 August 2024

of at least sixth order. In addition, the characterization of the domain interface is closely related to the gradient energy of the domain wall. Thus, for a precise and thorough understanding of the stability of polarization states and their associated domain walls, the Landau coefficients and gradient coefficients are required. However, it is important to recognize that determining or calculating these parameters is a major challenge in materials science. Currently, the number of materials for which Landau potentials are available is still very limited [26], which makes it difficult to investigate domain structure formation in materials without the required coefficients. For instance, scientists have discovered that semiconductor solar cells based on the organic metal halide framework could have ferroelectric properties. An illustrative example of this is the semiconductor methylammonium lead iodide ($MAPbI_3$) [27], which exhibits exceptional electronic properties at domain walls [28] and is therefore a promising candidate for state-of-the-art photovoltaic applications. However, the examination of domain formations and the mechanisms underlying their exceptional performance cannot be effectively explored through the phase-field approach, using the TDGL framework.

To avoid requiring Landau coefficients, we have introduced a novel model that utilizes the multiphase-field method for analyzing ferroelectric materials, as described in our recent publication [29]. In this approach, we use the phase-field concept $\boldsymbol{\phi}$ as an order parameter to represent different domains, ferroelectric phases or grains, and the domain structures are computed based on the phase transformations between different states of the order parameter. Using this novel methodology, we systematically investigated the domain formation, domain switching, polarization hysteresis, and strain hysteresis within the $BaTiO_3$ material system under external electric fields, including both single-crystal and polycrystalline systems. In the present study, we have further extended our multiphase-field model to compute the domain morphologies in ferroelectric thin films.

The film is constrained by a substrate, where the mobility of the substrate is maintained at zero throughout the simulation to ensure temporal constancy. Differing from the application of periodic boundary conditions typically applied to bulk materials, we implement specific mechanical and electric boundary conditions at the upper and lower boundaries of the system, so as to emulate the constraints encountered in a thin film scenario. Regarding the mechanical modeling, a jump condition approach [30] is employed within the diffuse interface. Using this method provides an accurate scheme for calculating the mechanical field across the film and substrate, allowing us to easily capture the misfit strain between the film and substrate. Besides, as $\boldsymbol{\phi}$ is the order parameter, we defined the structural stability by using a multi-obstacle potential, instead of the Landau potential in the TDGL model. This simplifies the input of the material coefficients. Furthermore, the gradient energy combined with the multi-obstacle potential describes interfacial energy. The interfacial energy parameter, used to characterize the domain wall properties, can be independently adjusted, allowing tailored modifications for different interfaces. This provides an accurate description of the properties of the domain wall and the film-substrate interface. Moreover, the purpose of this model is to compute domain structures based on the predetermined polarization state for each variant. The absence of updating polarization for each variant in ferroelectric phases during the simulation enhances computational efficiency, as a significantly large time scale factor can be chosen while maintaining system stability. The present model is based on the multiphase-field approach, which enables large-scale simulations, such as computations of martensite transformations in Ref. [31]. This manuscript begins with an explanation of the model, followed by an application of simulated thin film of the classic ferroelectric material PTO. The analysis includes the investigation of domain structures that are influenced by the deformation of the substrate, different substrate constraints, film thicknesses, and different temperature conditions.

2. Multiphase-field model for the prediction of domain structures in ferroelectric films

The basic concept underlying the multiphase-field approach for computing domain structures in ferroelectric thin films is visually depicted in Fig. 1. The present study focuses on the growth of a (001)-oriented PTO epitaxial single-crystal thin film on a (001)-oriented cubic substrate. The epitaxial PTO film, which has a vertical dimension film thickness (h_f) along the growth axis, is confined by a substrate with a permissible deformation height (h_s). Drawing on the principles of the phase-field methodology, a tuple $\boldsymbol{\phi} = \{\phi_1, \dots, \phi_N\}$ of N order parameters ϕ_α is introduced, which demarcates distinct regions with discernible physical attributes. This distinction facilitates the characterization of the substrate via the order parameter ϕ_{sub}, coupled with the introduction of ϕ_{film} to represent a film. In this scenario, which is demonstrated in Fig. 1(b), the order parameters within the spatial extent of the film area take the values $\phi_{\text{film}}(\boldsymbol{x}, t) = 1$ and $\phi_{\text{sub}}(\boldsymbol{x}, t) = 0$, while at the same time the values $\phi_{\text{film}}(\boldsymbol{x}, t) = 0$ and $\phi_{\text{sub}}(\boldsymbol{x}, t) = 1$ are maintained within the boundaries of the substrate area. Furthermore, a diffuse interface is used to delineate the transitional region extending from a thin film to the substrate. In this diffuse interface, ϕ_{sub} decreases smoothly from one to zero in the x_3-direction, while ϕ_{film} conversely increases from zero to one (Fig. 1(b)). This results in a small but finite transition region, in which a mixture of film and substrate phases occurs. To model the non-transformation between the film and the substrate region, their mobility of phase transformation is limited to zero. Furthermore, the thin film itself persists in different regions with individual polarization variants. Thus, ϕ_{film} is algebraically defined as the sum $\sum_{i=1}^{n} \phi_i$, where each ϕ_i denotes an order parameter corresponding to individual polarization variants, and n denotes the number of polarization variants inherent in the ferroelectric material, as described in Ref. [29]. Consequently, in the scenario of a single-grain thin film containing exclusively one ferroelectric phase, $N = n + 1$. In PTO system with a tetragonal ferroelectric phase, as shown in Fig. 1(c), n is set to six and the polarization variants are oriented along the $\langle 100 \rangle$-directions. In addition, domains aligned perpendicular to the substrate are classified as c-domains, while those aligned with the in-plane directions are referred to as a-domains in the present work (see Fig. 1(c)). Taking into consideration these concepts, it is noteworthy that our model can also simulate film growth on orientations such as (110) and (111). In such case, stable polarization stemming from low-symmetry phases like orthorhombic and monoclinic could be stable and lead to complex domain structures. The strategy employed involves rotating the respective variants.

In ferroelectric thin films, elastic and electrostatic energy play a decisive role in the formation and stabilization of domain structures. For example, when a ferroelectric material undergoes a polarization change, its lattice adapts, resulting in mechanical strain and deformation. This interaction is more intricate in thin films, due to substrate effects. Strains facilitate domain formation, and specific domain orientations help relax the lattice to minimize the elastic energy associated with deformation. In addition, the electrostatic energy, which is relevant for the alignment of the electric dipoles, influences the stability of the domain. The equilibrium between elastic and electrical energy determines the domain properties such as formation, size, shape, and wall dynamics. Therefore, to understand the domain structures in ferroelectric thin films, an approach is required that takes into account not only the interfacial energies inherent to the domain wall properties within the multiphase-field methodology, but also the bulk driving forces arising from the elastic and electrical influences. This leads to the formulation of a total free energy of volume V for the thin film system, denoted as:

$$\mathcal{F} = \int_V f_{\text{grad}}(\nabla\boldsymbol{\phi}) + f_{\text{ob}}(\boldsymbol{\phi}) + f_{\text{elast}}(\boldsymbol{\phi}, \boldsymbol{\varepsilon}, \boldsymbol{P}) + f_{\text{elec}}(\boldsymbol{P}, \boldsymbol{E})\, \mathrm{d}V, \tag{1}$$

which relies on the multiphase-field method described by Nestler et al. [32].

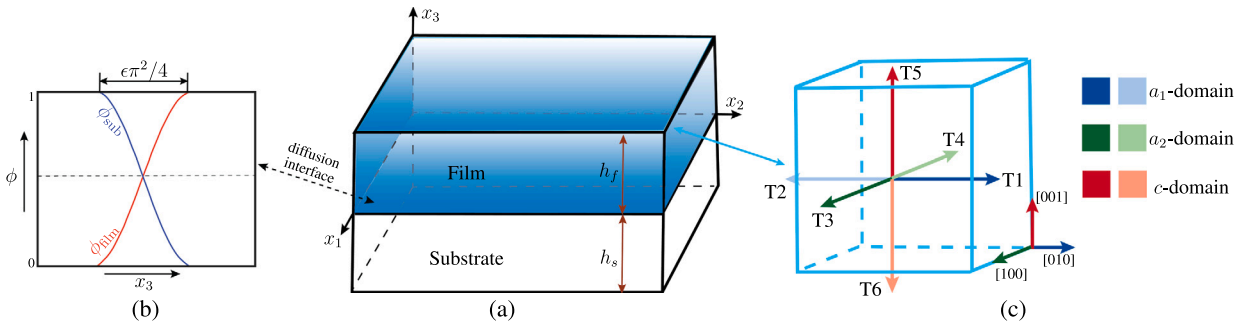

Fig. 1. Diagram showing the computational framework for computing domain structures in an epitaxial ferroelectric thin film. (a) The model description; (b) A description of the thin film and the substrate over the diffusion region, where $\epsilon\pi^2/4$ captures the interface thickness; (c) The orientation of the polarization variants in the PTO film.

The initial two terms on the right-hand side of Eq. (1) constitute the interfacial energy density, in which $f_{\text{grad}}(\nabla\boldsymbol{\phi})$ denotes the gradient energy density and $f_{\text{ob}}(\boldsymbol{\phi})$ is the multi-obstacle-type potential energy density. These two terms not only describe the interface profile between the film and the substrate, but also capture the properties of the domain walls between different polarization variants.

With $\gamma^{\alpha\beta}$ as the isotropic interfacial energy density and depending on Ref. [33], the gradient energy density can be formulated as:

$$f_{\text{grad}}(\nabla\boldsymbol{\phi}) = -\epsilon \sum_{\alpha,\beta>\alpha} \gamma^{\alpha\beta} \nabla\phi_\alpha \cdot \nabla\phi_\beta, \tag{2}$$

in which ϵ is a numerical parameter that scales the interface thickness as $\pi^2/4\,\epsilon$ in an equilibrium interface profile with the application of an obstacle potential.

The multi-obstacle potential can be expressed as:

$$f_{\text{ob}}(\boldsymbol{\phi}) = \begin{cases} \dfrac{16}{\epsilon\pi^2} \sum\limits_{\alpha<\beta} \gamma^{\alpha\beta}\phi_\alpha\phi_\beta & \text{if } \boldsymbol{\phi} \in \mathcal{G} \\ \infty & \text{else.} \end{cases} \tag{3}$$

$\mathcal{G}$ is the Gibbs simplex, conforming to the definition $\mathcal{G} = \{\boldsymbol{\phi} | \sum_\alpha \phi_\alpha = 1, \text{and } \phi_\alpha \geq 0\}$.

In the present study, the phase-dependent bulk energies, namely the elastic energy density (f_{elast}) and the electrostatic energy density (f_{elec}) are interpolated with a function, denoted as $h^\alpha(\boldsymbol{\phi}) = \phi_\alpha$, resulting in:

$$f_{\text{elast}} = \sum_\alpha f^\alpha_{\text{elast}} h^\alpha(\boldsymbol{\phi}) \quad \text{and} \quad f_{\text{elec}} = \sum_\alpha f^\alpha_{\text{elec}} h^\alpha(\boldsymbol{\phi}). \tag{4}$$

It is noteworthy that the identical interpolation function $h^\alpha(\boldsymbol{\phi})$ also describes the polarization change along the interface, which can be expressed as: $\boldsymbol{P} = \sum \boldsymbol{P}^\alpha h^\alpha(\boldsymbol{\phi})$. $\boldsymbol{P}^\alpha$ denotes the polarization vector of ϕ_α, where its magnitude $|P^\alpha|$ is defined by the spontaneous polarization of the material, namely, $|P^\alpha| = 75.7\,\mu\text{C}\,\text{cm}^{-2}$.

2.1. Multiphase elasticity model and density of elastic free energy

As already mentioned, the mechanical driving force plays a crucial role in the calculation of domain structures in ferroelectric materials. This role is particularly pronounced when it comes to epitaxial films that are constrained by substrates. The inherent properties of the substrate, which include factors such as its crystalline structure and its coefficient of thermal expansion, lead to a misfit strain between the thin film and the substrate. Such a strain leads to considerable changes in the energy landscape of the domains and thus has a major influence on their behavior, in terms of switching, dimensions, and orientation. Therefore, it is essential to accurately replicate the misfit strain between the substrate and the film, as well as its consequential impact on the driving forces in the transition region between the different ferroelectric variants. In this study, we use a multiphase elasticity model that is able to fulfill the mechanical jump conditions, as proposed and referenced in Refs. [31,34,35].

In general, the strain energy density of the phase α can be formulated as follows:

$$f^\alpha_{\text{elast}}(\boldsymbol{\varepsilon}^\alpha, \boldsymbol{P}^\alpha) = \frac{1}{2}\left[(\boldsymbol{\varepsilon}^\alpha - \tilde{\boldsymbol{\varepsilon}}^\alpha) \cdot \boldsymbol{C}^\alpha \cdot (\boldsymbol{\varepsilon}^\alpha - \tilde{\boldsymbol{\varepsilon}}^\alpha)\right], \tag{5}$$

where $\boldsymbol{C}^\alpha$ represents the elastic stiffness of the material, a property that depends on the specific ferroelectric phase. Concurrently, $\boldsymbol{\varepsilon}^\alpha$ denotes the total strain that is particular to the respective phase, while $\tilde{\boldsymbol{\varepsilon}}^\alpha$ corresponds to the inelastic strain component of $\boldsymbol{\phi}$. With $\boldsymbol{u}$ representing the displacement vector, $\boldsymbol{\varepsilon}$ is defined as $\boldsymbol{\varepsilon} = \frac{1}{2}\left(\nabla\boldsymbol{u} + (\nabla\boldsymbol{u})^{\text{T}}\right)$, capturing the symmetric part of the displacement gradient $\nabla\boldsymbol{u}$. Following the approach in Refs. [34–37], we decompose the strain tensor into $\boldsymbol{\varepsilon} = \sum_\alpha \boldsymbol{\varepsilon}^\alpha h^\alpha(\boldsymbol{\phi})$, and thus into a linear interpolation of the phase-inherent strains. A corresponding volumetric decomposition of stresses, denoted as $\boldsymbol{\sigma}$, can similarly be defined as $\boldsymbol{\sigma} = \sum_\alpha \boldsymbol{\sigma}^\alpha h^\alpha(\boldsymbol{\phi})$. The nonelastic strain $\tilde{\boldsymbol{\varepsilon}}^\alpha$ comprises both the spontaneous strain $\boldsymbol{\varepsilon}^{\alpha,0}(\boldsymbol{P}^\alpha)$ and the misfit strain $\boldsymbol{\varepsilon}^{\text{mis}}$, which results in:

$$\tilde{\boldsymbol{\varepsilon}}^\alpha = \boldsymbol{\varepsilon}^{\alpha,0}(\boldsymbol{P}^\alpha) + \boldsymbol{\varepsilon}^{\text{mis}}. \tag{6}$$

The spontaneous strain $\boldsymbol{\varepsilon}^{\alpha,0}(\boldsymbol{P}^\alpha)$, represented by the Einstein summation convention, is:

$$\varepsilon^{\alpha,0}_{ij} = Q_{ijkl} P^\alpha_k P^\alpha_l, \tag{7}$$

where $\boldsymbol{Q}^\alpha$ are the electrostrictive coefficients which are characteristic for each ferroelectric phase. The reason for the misfit strain lies in the different crystal structures of the film and substrate. This phenomenon leads to a tangential interface strain, which can be represented mathematically as follows:

$$\begin{aligned} \varepsilon^{\text{mis}}_{11} &= \varepsilon^{\text{mis}}_{22} = \frac{a_{\text{s}} - a_{\text{f}}}{a_{\text{f}}}, \\ \varepsilon^{\text{mis}}_{12} &= \varepsilon^{\text{mis}}_{i3} = 0\,(i = 1, 2, 3), \end{aligned} \tag{8}$$

where a_{f} and a_{s} denote the lattice parameters of the film and substrate, respectively. The mechanical jump condition approach is used to address the mechanical field within the system. This method uses normal stress components and tangential strain components to define a consistent potential type and thus facilitates the formulation of the driving force. For an overview of this method, the reader is referred to Appendix A. A detailed description of this approach can be found in Refs. [34,38].

2.2. Electrostatic energy model

The electric energy density of a phase α with polarization $\boldsymbol{P}^\alpha$ is calculated by

$$f_{\text{elec}}(\boldsymbol{P}^\alpha, \boldsymbol{E}) = -P_i E_i - \frac{1}{2}\kappa_0 \kappa_{ij} E_i E_j \tag{9}$$

in which $\kappa_0 = 8.85 \times 10^{-12}\,\text{F}\,\text{m}^{-1}$ denotes the absolute dielectric permittivity, while κ_{ij} is recognized as the background dielectric permittivity [39] with $\kappa_{ij} = 0$ when $i \neq j$. The symbol E_i in Eq. (9) denotes a component of the electric field that is defined by $\boldsymbol{E} = \boldsymbol{E}_D + \boldsymbol{E}_{ext}$. $\boldsymbol{E}_{ext}$

represents the external electric field, and $\boldsymbol{E}_D$ is the depolarization field, which is described by the relationship $E_{D,i} = -\psi_{,i}$. The determination of ψ, the electric potential, is facilitated by the solution of a Poisson equation, which reads:

$$\kappa_0 \kappa_{ij} \Delta\psi = \nabla \cdot \boldsymbol{P}^{\alpha}. \tag{10}$$

This equation is underpinned by the connection between $E_{D,i}$ and the electrical displacement D_i, which is expressed by the relationship $D_i = \kappa_0 \kappa_{ij} E_{D,j} + P_i$. The solution for the electrical potential is only performed in the thin film, *i.e.,* for $x_3 > 0$, while it is assumed to be constant in the substrate. Thus, the corresponding boundary conditions are applied at the interface between the film and the substrate.

To characterize the electric field distribution at the lower ($x_3 = 0$) and the upper ($x_3 = h_f$) interface of the film, two different forms of electrical boundary conditions are used, namely short-circuited and open-circuited boundary conditions. The short-circuited boundary condition has the property that the electrical potential ψ is given on both film surfaces, represented as:

$$\psi|_{x_3=0} = \psi_1,\ \psi|_{x_3=h_f} = \psi_2. \tag{11}$$

Assuming an absence of internal space charge inside the film, the quantity D_i conforms to the electrostatic equilibrium equation $D_{i,i} = 0$. On the top and bottom surfaces of the film, the condition

$$D_3|_{x_3=0,\, x_3=h_f} = 0 \tag{12}$$

characterizes an open-circuited scenario. Letters i and j mentioned above follow the summation convention for repeated indices, with their values ranging from 1 to 3.

2.3. Governing equations

Based on the works of Refs. [31,33,40], the minimization of the energy functional (Eq. (1)) with a variational approach leads to the calculation of the domain structure, which is performed according to the order parameter ϕ_α:

$$\frac{\partial \phi_\alpha(\boldsymbol{x},t)}{\partial t} = -\frac{1}{\widetilde{N}\epsilon} \sum_{\beta \neq \alpha}^{\widetilde{N}} \left[M^{\alpha\beta} \left(\frac{\delta \mathcal{F}_{\text{int}}}{\delta \phi_\alpha} + \epsilon \hat{\alpha}(\phi_\alpha, \boldsymbol{\nabla}\phi_\alpha) - \frac{\delta \mathcal{F}_{\text{int}}}{\delta \phi_\beta} - \epsilon \hat{\alpha}(\phi_\beta, \boldsymbol{\nabla}\phi_\beta) - \frac{8\sqrt{\phi_\alpha \phi_\beta}}{\pi} \Delta^{\alpha\beta} \right) \right], \tag{13}$$

where $M^{\alpha\beta}$ is known as the phase-field mobility for the phases α and β, and $\widetilde{N}$ denotes the number of the locally active phases. $\mathcal{F}_{\text{int}}$ represents the interfacial energy, comprising both gradient energy and obstacle potential terms. Meanwhile, $\Delta^{\alpha\beta}$ is defined as:

$$\Delta^{\alpha\beta} = \left(\frac{\delta}{\delta \phi_\alpha} - \frac{\delta}{\delta \phi_\beta} \right) \mathcal{F}_{\text{bulk}} \tag{14}$$

where $\mathcal{F}_{\text{bulk}}$ denotes the bulk contribution, encompassing elastic and electrostatic energy components. $\epsilon\hat{\alpha}(\phi_\alpha, \nabla\phi_\alpha)$ is defined as:

$$\epsilon \hat{\alpha}(\phi_\alpha, \nabla\phi_\alpha) = \epsilon \gamma_\alpha^c \left(\Delta\phi_\alpha - |\nabla\phi_\alpha| \nabla \cdot \left(\frac{\nabla\phi_\alpha}{|\nabla\phi_\alpha|} \right) \right), \tag{15}$$

which avoids a dynamic curvature minimization to ensure a correct interaction of the gradient and the potential energy density. γ_α^c can be understood as a factor that calibrates the strength of the artificially constructed interface. For more comprehensive information, the reader is advised to refer to the Refs. [29,31].

$\delta\mathcal{F}/\delta\phi_\alpha$ is the variational derivative of the total energy, with respect to ϕ_α, defined by:

$$\frac{\delta \mathcal{F}}{\delta \phi_\alpha} = \frac{\partial f}{\partial \phi_\alpha} - \boldsymbol{\nabla} \cdot \frac{\partial f}{\partial \nabla \phi_\alpha}, \tag{16}$$

where f could be f_{grad}, f_{ob}, f_{elast}, and f_{elec}. This definition allows us to easily derive the electrostatic driving force $\boldsymbol{\Delta}_{\text{elec}}^{\alpha\beta}$ as:

$$\boldsymbol{\Delta}_{\text{elec}}^{\alpha\beta} = f_{\text{elec}}^{\beta} \frac{\partial h^{\beta}(\boldsymbol{\phi})}{\partial \phi_\beta} - f_{\text{elec}}^{\alpha} \frac{\partial h^{\alpha}(\boldsymbol{\phi})}{\partial \phi_\alpha}. \tag{17}$$

In addition to the phase-field evolution equation, the variation method provides the stationary momentum balance

$$\nabla \cdot \bar{\boldsymbol{\sigma}} = \boldsymbol{0} \tag{18}$$

as an additional condition to minimize the free energy functional (1). The solution of the momentum balance provides knowledge of the displacement field $\boldsymbol{u}$ and thus about the total strain. According to Ref. [30,31,35], the elastic free energy density is evaluated by the Legendre transformation, which gives a comprehensive elastic potential $W(\boldsymbol{\sigma}_n, \boldsymbol{\epsilon}_t, \boldsymbol{\phi})$ that depends on continuous variables. Consequently, this transformation leads to the following formulation of the mechanical driving force:

$$\boldsymbol{\Delta}_{\text{elast}}^{\alpha\beta}(\boldsymbol{\sigma}_n, \boldsymbol{\epsilon}_t, \boldsymbol{\phi}) = \frac{\partial W(\boldsymbol{\sigma}_n, \boldsymbol{\epsilon}_t, \boldsymbol{\phi})}{\partial \phi_\beta} - \frac{\partial W(\boldsymbol{\sigma}_n, \boldsymbol{\epsilon}_t, \boldsymbol{\phi})}{\partial \phi_\alpha}, \tag{19}$$

with the overall elastic potential $W(\boldsymbol{\sigma}_n, \boldsymbol{\epsilon}_t, \boldsymbol{\phi})$ depending on the interface normal stress $\boldsymbol{\sigma}_n$ and the tangential strain $\boldsymbol{\epsilon}_t$ (see Appendix A for details).

2.4. Advantages and limitations of the proposed approach

In the TDGL model, the polarization is used as the order parameter, and domain structures are calculated by minimizing the energy functional with respect to polarization. Consequently, the polarization vector evolves over time, resulting in an inhomogeneous distribution of the polarization vector even within a single domain. Since the TDGL model solves for the polarization itself based on the Landau-Devonshire Theory framework, it could be used to predict equilibrium polarizations and thus for calculating misfit strain–temperature phase diagrams [12]. In contrast, in the proposed model, the polarization state of each variant is defined as an input. Therefore, the polarization within each variant remains homogeneous. As both the orientation and magnitude of polarization are predefined for each variant of ferroelectric phases in our model with the current format, the calculation of the misfit strain–temperature phase diagram is not feasible. Instead, to explore domain structures of films at specific temperatures alongside corresponding misfit strains, we can rely on such a phase diagram to predetermine the polarization state for each variant. Experimental determinations or theoretical simulations, such as Density Functional Theory calculations, could also provide the necessary data regarding the polarization states of ferroelectric variants. Furthermore, since the evolution of the polarization state for each variant is predefined, we do not require Landau potential to drive the stable polarization state, simplifying the computational coefficients in our model and enhancing computational efficiency. Additional details can be found in the Introduction or Ref. [29].

3. Simulation setup and numerical procedure

We perform all simulations using our proprietary software Pace3D (Parallel Algorithms for Crystal Evolution in 3D) [41]. In this framework, we use a finite difference algorithm that includes an explicit forward Euler scheme to solve the phase-field evolution equation (Eq. (13)), which allows us to determine the configuration of the domain. For the spatial discretization of all governing equations, an equidistant Cartesian grid is used. The flowchart in Fig. 2 provides an overview of the solution process used in the subsequent simulations. Both the mechanical and the electrostatic equilibrium (Eqs. (10) and (18)) are solved at each time step by applying the conjugate gradient method. The initial setup for the thin film systems was created using the Voronoi tessellation. To increase the computational efficiency during the simulation, we partitioned the domain in both the x_1- and x_2-directions by using the message passing interface (MPI) standard. The computational analysis of domain structures within a thin film system relies on the specification of well-defined boundary conditions to solve variables encompassing phase-field tuple $\boldsymbol{\phi}$, the electric field, and the

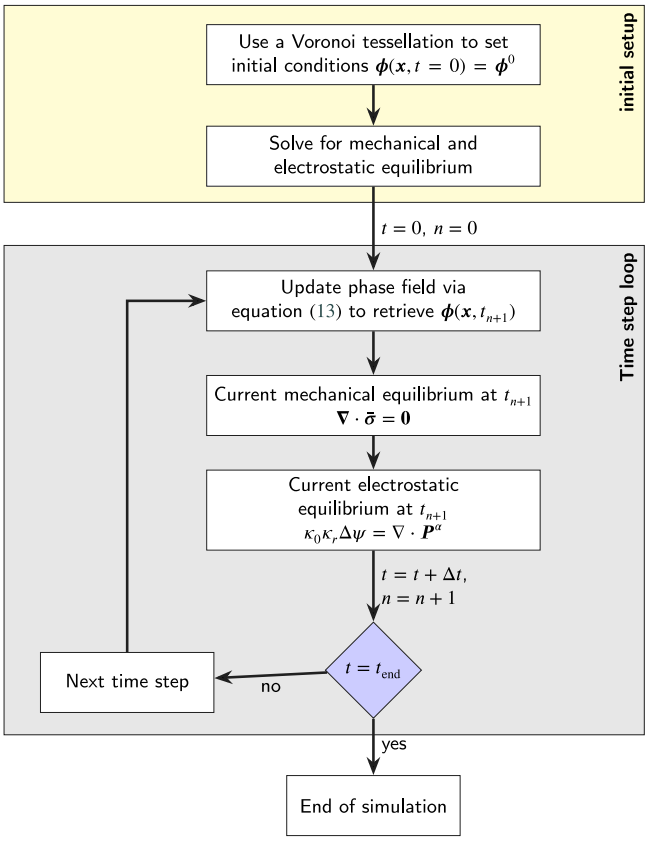

Fig. 2. Overview of the solution procedure for the numerical simulations.

mechanical fields. For all fields, periodic boundary conditions are prescribed along the x_1- and x_2-axes. With regard to the phase field, the Neumann boundary condition $\nabla\phi \cdot e_3 = 0$, where e_3 denotes the unit vector in the x_3-direction, is invoked for the upper ($x_3 = h_f$) and lower ($x_3 = 0$) surfaces of the thin film, which results in all interfaces being perpendicular to the boundary of the film. Since the polarization is predetermined and interpolated in each cell by ϕ, such a boundary condition aligns with a Neumann boundary condition for the polarization. This boundary specification suggests that the electric potential ψ at the boundary is zero, which means that there is no flux of electric charge across the boundary. Correspondingly, a short-circuited boundary condition is applied to the top and bottom surfaces of the film to solve the depolarization field. Moreover, in terms of mechanics on the top and bottom surfaces, a condition of $\sigma_{i3} = 0$ is enforced at $x_3 = h_f$ to emulate a stress free interface, while keeping the substrate at the bottom layer of the system in a fixed position, by imposing a vanishing displacement $u|_{x_3=-h_s} = 0$.

In this study, PTO serves as a simulated material corresponding to a tetragonal ferroelectric phase that can form either 90° or 180° domain walls. Taking the interface stability into account, ϵ was set to a value of $2\Delta x_1$. The interfacial energy $\gamma^{\alpha\beta}$ is calculated according to the expression $\gamma^{\alpha\beta} = 1.26|\alpha_1|l_0 P_0^2$ [42]. Here, α_1 represents the dielectric stiffness at room temperature, while l_0 is determined by the gradient coefficient G_{11}, using the formula $l_0 = \sqrt{G_{11}/(0.6|\alpha_1|)}$. Additionally, the domain was discretized into cells with uniform dimensions of $\Delta x_1 = \Delta x_2 = 1\,\text{nm}$ and $\Delta x_3 = 0.5\,\text{nm}$. The mobility coefficient $M^{\alpha\beta}$, which governs the mobility of the ferroelectric variants within the film, was set to one. The simulation starts with the calculation of domain structures formation under various constraints for model validation, followed by the computation of epitaxial PTO growth on

Table 1
The phase-field parameters and material coefficients used in the simulation.

Material coefficients	Symbol	Value	Unit
Dielectric stiffness	α_1	(T-497)*3.8[a]	10^5 [m F^{-1}]
Interfacial energy	$\gamma_{\alpha\beta}$	0.01	J m^{-2}
–	γ^e_{α}	0.01	J m^{-2}
Phase-field mobility	$M^{\alpha\beta}$	1	–
Elastic tensor C	C_{11}	17.46	10^{10} [N m^{-2}]
PTO	C_{12}	7.94	10^{10} [N m^{-2}]
	C_{44}	11.11	10^{10} [N m^{-2}]
Electrostrictive tensor Q	Q_{11}	8.90	10^{-2} [m^4 C^{-2}]
PTO	Q_{12}	−2.60	10^{-2} [m^4 C^{-2}]
	Q_{44}	6.75	10^{-2} [m^4 C^{-2}]
Elastic tensor C	C_{11}	43.10	10^{10} [N m^{-2}]
KTO[b]	C_{12}	10.30	10^{10} [N m^{-2}]
	C_{44}	10.90	10^{10} [N m^{-2}]
Gradient coefficient	G_{11}	10.56	10^{-11} [N m^4 C^{-2}]
Thermal expansion[c]	α_f	12.60	10^{-6} [K^{-1}]
	α_s	6.67	10^{-6} [K^{-1}]

[a] For PTO, the values for α_1, C, and Q are taken from Ref. [12].
[b] For KTO, the values for C are taken from Ref. [43].
[c] α_f and α_s are taken from Ref. [44].

the (001)-oriented $KTaO_3$ (KTO) substrate to investigate the influence of film thickness and temperature on the domain morphology. The material coefficients required in the current simulation are listed in Table 1. To increase accuracy, the input coefficients were converted into dimensionless values. The corresponding transformation process can be found in Ref. [29].

4. Results and discussion

4.1. Influence of substrate deformation on the domain structures

By a systematic simulation study, we investigated the influence of the substrate height h_s on the volume fraction of domains and the morphology of domains at room temperature, within a thin film subject to a specific tensile misfit strain, represented as $\epsilon^{\text{mis}} = 0.006$. In the context of our model, the variable h_s delineates the region of the substrate in which a deformation is permissible, while at $x_3 = -h_s$, a zero displacement is prescribed by appropriate boundary conditions. In the special case where $h_s = 0$, this corresponds to a scenario characterized by a completely rigid substrate. The initial configuration of a quasi-2D thin film system was established as shown in Fig. 3(a), which is discretized with $128 \times 1 \times (40 + n_s)$ cells, where $n_s = h_s/\Delta x$ is the number of cells discretizing the substrate, which depends on the considered substrate height h_s. The substrate height h_s was allowed to vary in a range from 0 to $33\Delta x_3$, with an internal step size of $3\Delta x_3$. In this setup, six different polarization states were randomly distributed within film region, each of which is represented by a corresponding black arrow. The dots and crosses in the T3 and T4 variants respectively indicate their polarization direction towards or away from the observer.

The graphical representation of the calculated volume fraction of the c-domain within the film, denoted as V_c, is shown in Fig. 3(b) for different substrate heights h_s at the equilibrium stage. It can be seen that as the substrate height (h_s) increases, the parameter V_c decreases and finally converges to a constant value when h_s becomes sufficiently large, indicating that the influence of the displacement boundary condition at $x_3 = -h_s$ on the domain evolution becomes negligible. To explain the background of this phenomenon, we have generated a plot showing the average bulk driving force $f^*_{\text{bulk}} = f^*_{\text{elast}} + f^*_{\text{elec}}$ and its elastic contribution f^*_{elast} of the thin film as a function of the substrate height (see Fig. 3(b)). Remarkably, the analysis shows that both the elastic energy and the total bulk energy, which is the sum of the elastic and electrostatic energy, show a decreasing trend with increasing h_s. This means that the driving force resulting from the elastic energy promotes the stability of the a-domain at different substrate heights.

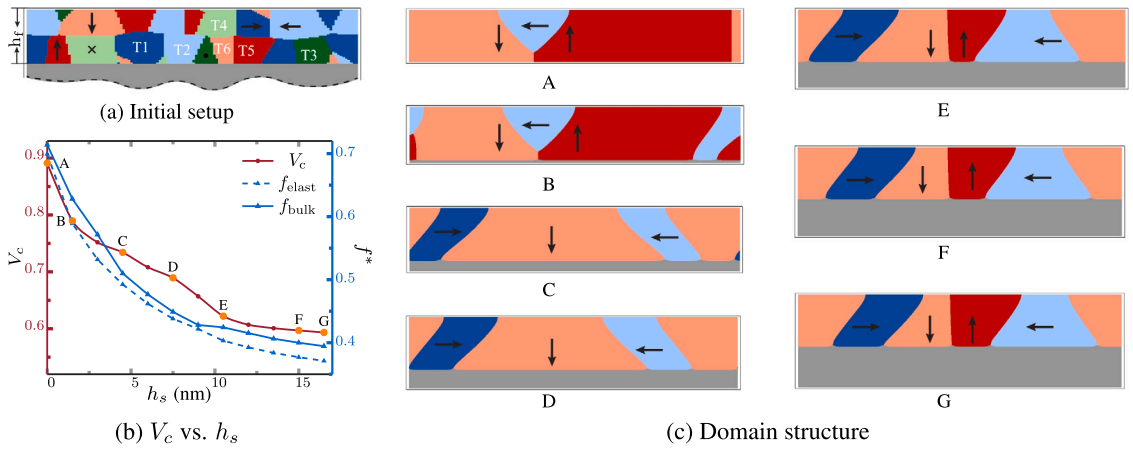

Fig. 3. (a) shows the initial setup of the quasi-2D film system. (b) represents the computed volume fraction of the c-domain (V_c), the elastic energy (f^*_{elast}), along with the summation of elastic and electrostatic energies (f^*_{bulk}). (c) shows the domain structures corresponding to the marked substrate heights (h_s), denoted from A to G in (b).

The deformation of the substrate is due to the non-uniform deformation within the thin film, which causes the displacements in the substrate to approach zero at a sufficient distance from the interface. This phenomenon, in turn, contributes to a reduction in elastic energy density, which consequently leads to a decrease in the volume fraction of the c-domain.

Fig. 3(c) A–G shows the associated domain morphology corresponding to the distinct h_s values marked in Fig. 3(b). It is evident that the morphology of the domain changes as the substrate height varies, but eventually stabilizes in a consistent configuration, once the substrate height reaches a convergent value that alters V_c only slightly. In addition, the height of the substrate has a recognizable influence on the domain morphology. At a substrate height of $h_s = 0$ (case A), the a-domain cannot exist in the immediate vicinity of the film–substrate interface. Even for relatively large values of h_s, ranging from $3\Delta x_3$ to $15\Delta x_3$ (case B to D), the width of the a-domains near the film–substrate surface is slightly narrower. Additionally, it is observed that T2 emerges when the substrate height reaches 4.5 nm. Consequently, as shown from case E to case G, both the 90° and 180° domain walls stabilize with increasing substrate height, while the orientation of the domain walls between the a-domains and the c-domains deviates slightly from the ideal 45° angle relative to the film–substrate interface.

It is noteworthy that the motivation behind conducting this comparative computation lies in determining the critical substrate height, which was found to be $h_s = 0.6h_f$ from the simulation. Above this threshold, the influence of substrate deformation converges to a specific value. In the context of large-scale simulations, the identification of this critical value is of central importance, as it shows that substrate heights exceeding this threshold have a negligible influence on the resulting domain structures. Thus, by identifying this critical height as a key parameter to determine the substrate thickness relative to the film, we can achieve efficient use of computing resources. Drawing from the insights gained in the present simulations, in subsequent simulations, we maintain the substrate thickness h_s at a value corresponding to $0.75h_f$.

4.2. Effects of substrate constraints on volume fractions and the morphology of domains

In this subsection, we performed 3D simulations with a grid size of $128 \times 128 \times 70$ cells (with a film thickness $h_f = 40\Delta x_3 = 20$ nm and accordingly a representative substrate height $h_s = 30\Delta x_3 = 15$ nm) to investigate the effects of substrate constraints on the domain fraction and configuration at room temperature. The initial 3D setup, the domain morphologies, the computed V_c (second row), and the average $\bar{\varepsilon}_{33}$ (third row) with varying constraints, due to the substrate, are shown in Fig. 4. Each color in the thin film representation in Fig. 4 corresponds to a specific tetragonal variant, analogous to the representation in Fig. 3. Additionally, the polarization orientation for each variant can be cross-referenced with Fig. 1.

From the observations in Fig. 4, it becomes evident that the misfit strain exerts a profound influence on both the domain structures and the stability of polarization variants with varying orientations. For instance, the c-domain does not remain stable under the condition of a considerable tensile strain ($\varepsilon^{\text{mis}} = 0.012$). As a result, all domain walls between a_1- and a_2-domains are oriented perpendicular to the film surface and follow the crystallographic directions [110] or [1$\bar{1}$0]. With a reduction in the magnitude of ε^{mis}, (*i.e.*, a reduction in the size of the tensile stress), the c-domain begins to manifest itself, which leads to an increase in the volume fraction of the c-domains. Consequently, the equilibrium domain structures include all two domain types, and the orientations of the domain walls between a- and c-domains show a slight deviation from the 45° direction relative to the film–substrate interface. If the film is subjected to a compressive misfit strain with an amplitude of 0.003 or more, the a-domains are completely missing. The domain morphologies for misfits of $\varepsilon^{\text{mis}} \geq 0.01$ exhibit the typical 90° configurations of tetragonal compositions. The polarization vectors are aligned in the plane of the film, which results in this characteristic stripe pattern. Misfits of $\varepsilon^{\text{mis}} \leq -0.001$ exhibit typical watermark domain morphologies, originating from 180° domain configurations. In the two different domain variants shown here, the polarization vector is aligned outside the film plane, resulting in the typical meandering domain walls. It is noteworthy that the critical thresholds for the absolute magnitudes of tensile and compressive strains, required to maintain either a-domains or c-domains, do not coincide. The disparity can be attributed to the imposition of short-circuited boundary conditions at both the upper and lower surfaces of the thin film. This observation is in accordance with previous results from TDGL-based phase-field simulations, which support the idea that the application of short-circuited boundary conditions increases the stability of c-domains [8].

The average $\bar{\varepsilon}_{33}$ in the $\bar{\varepsilon}_{33}$ vs. ε^{mis} plot of Fig. 4 shows a remarkable increase with the shift of the misfit strain from the tensile to the compressive state, possibly favoring the stability of the c-domain. Consequently, the observed trend in V_c versus ε^{mis} mirrors that of $\bar{\varepsilon}_{33}$ versus ε^{mis}. It should be noted that due to the imposition of periodic boundary conditions on the x_1- and x_2-axes, both ε_{11} and ε_{22} are equal to zero on average. These components are therefore not taken into account in this paper. To gain insight into the mechanisms of domain structures formation subjected to different constraint by the substrate, we have elucidated the temporal progression of domain formation at misfit strain values of $\varepsilon^{\text{mis}} \in \{0.012, 0.006, -0.003\}$, as shown in Figs. 5 to 7.

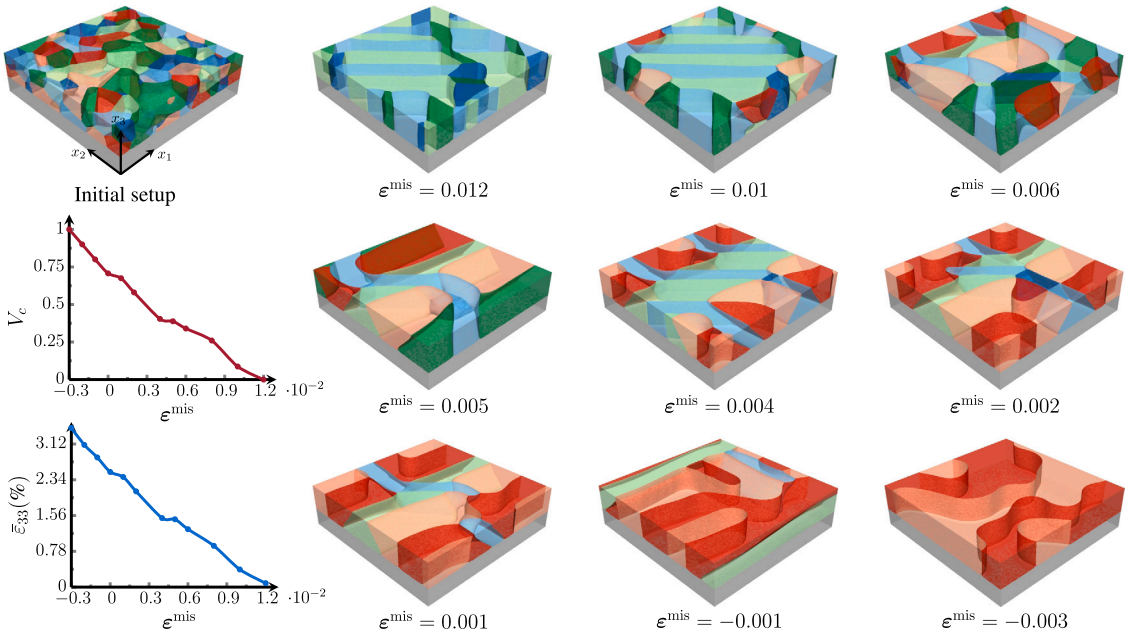

Fig. 4. Variations of the domain configurations, the volume fraction of the c-domain, and ε_{11}^{-}, under different misfit strain conditions.

To compare the influence of varying constraints on the final domain morphology, the evolution of the principal strains, namely ε_{11}, ε_{22}, and ε_{33}, has also been included in Figs. 5 to 7 for each respective case.

In the presence of a significant tensile strain $\varepsilon^{\mathrm{mis}} = 0.012$ (as shown in Fig. 5), the observation of the gradual disappearance of c-domains over time implies that substrate confinement exerts a favorable influence on the preferential formation of a-domains, consistent with the above discussion. By examining the evolution of the principal strain, a noticeable reduction in ε_{33} can be observed. When reaching the equilibrium state, it becomes evident that only the two principal strains oriented along the direction of the a-domain are present. This observation underlines the idea that elastic driving forces strongly promote the formation of the a-domain with large tensile constraints.

When the misfit strain is reduced from $\varepsilon^{\mathrm{mis}} = 0.012$ to $\varepsilon^{\mathrm{mis}} = 0.006$, the temporal evolution shown in Fig. 6(a) revels the coexistence of all polarization states, which leads to the formation of a complex domain morphology. In this scenario, the presence of all principal strains is evident, as shown in Figs. 6(b)–(d). In contrast to the tensile constraint, an appropriately applied compressive constraint from the substrate ($\varepsilon^{\mathrm{mis}} = -0.003$) results in a reduction of the a-domains, as shown in Fig. 7(a). Compared to Fig. 5(a), difference in the misfit strain leads to a complete change in stability of a- and c-domains during the transformation of the variants, which ultimately characterizes the domain morphology with the exclusive presence of c-domains. In this case, the gradients of ε_{11} and ε_{22} disappear, which means that the compressive constraint strengthens the elastic driving force that favors c-domains, while it becomes weaker for a-domains.

So far, our model has undergone a thorough validation to evaluate its ability to predict domain structures under the influence of substrate deformations and constraints. The simulated results in this study are consistent with previous research using the TDGL model, as documented in Refs. [8,12]. Therefore, in the following subsections, we will investigate the domain structures related to PTO growth on the actual substrate KTO.

4.3. Impact of film thickness on domain structures

In further simulation studies, we focused on the growth of (001)-oriented PTO films on KTO substrates, using a computational grid with 128 cells along the x_1- and x_2-axes, while the film thickness was systematically varied. In the above simulations, it was assumed that the ferroelectric film is completely constrained by the underlying substrate. This assumption led to the emergence of internal stresses, due to epitaxy, as well as spontaneous stresses, due to the ferroelectric phase transition. However, considerations of thickness-dependent phenomena, such as strain relaxation, were not taken into account. If the internal stresses caused by the misfit of the lattice exceed a critical threshold, these stresses are immediately relaxed. Consequently, the aforementioned assumption becomes inappropriate under conditions where internal stresses are excessively large, which may overestimate the misfit strain. To address this issue, we considered the misfit strain as a thickness-dependent strain, which is denoted as $\varepsilon_{ij}^{\mathrm{mis}}(h)$ and is expressed as follows:

$$\varepsilon_{ij}^{\mathrm{mis}}(h) = 1 - \frac{1 - \tilde{\varepsilon}_{ij}^{0}}{1 - \tilde{\varepsilon}_{ij}^{0}(1 - h_c/h)} \; (i = j = 1, 2) \tag{20}$$

at room temperature [45]. $\tilde{\varepsilon}_{ij}^{0}$ represents the ideal misfit strain at room temperature, and its calculation is determined by Eq. (8), where $\tilde{\varepsilon}_{11}^{0}$ and $\tilde{\varepsilon}_{22}^{0}$ are the only non-vanishing strain components. From the lattice parameters of cubic unstrained PTO (3.956 Å) and KTO (3.989 Å) [15], the ideal misfit strain $\tilde{\varepsilon}_{ij}^{0}$ for PTO on KTO is estimated to be 0.83 % at room temperature. h_c in Eq. (20) designates the critical thickness for dislocation formation, and its computation is derived from a People–Bean (PB) model [46,47]. For a detailed understanding, it is advisable to refer to the information provided in Refs. [15,46,47]. Using the PB model and Eq. (20), the critical thickness corresponding to $\tilde{\varepsilon}_{ij}^{0} = 0.83\%$ as well as the actual strain associated with the film thickness can be derived during the growth of PTO on KTO. Further insights and graphical representations can be found in Fig. 1 and 3 of Ref. [15], which serve as essential references for the inputs used in this simulation.

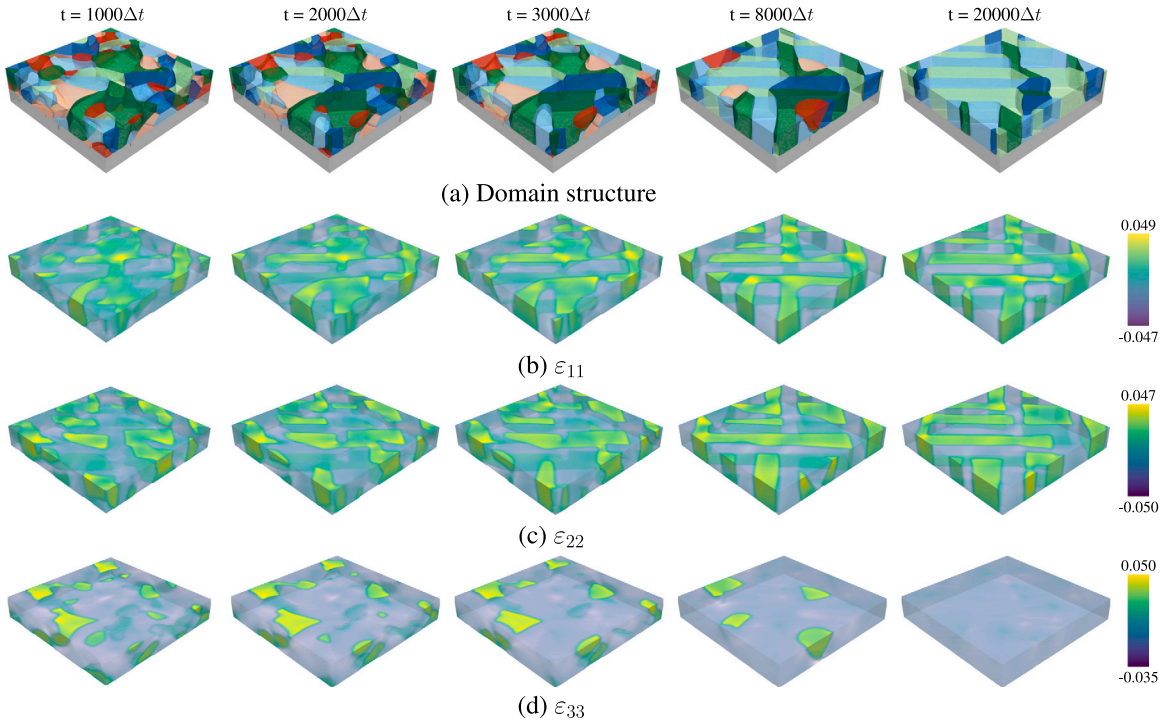

Fig. 5. The temporal evolution of domain structures, together with the corresponding ϵ_{11}, ϵ_{22}, and ϵ_{33}, at $\epsilon^{\text{mis}} = 0.012$.

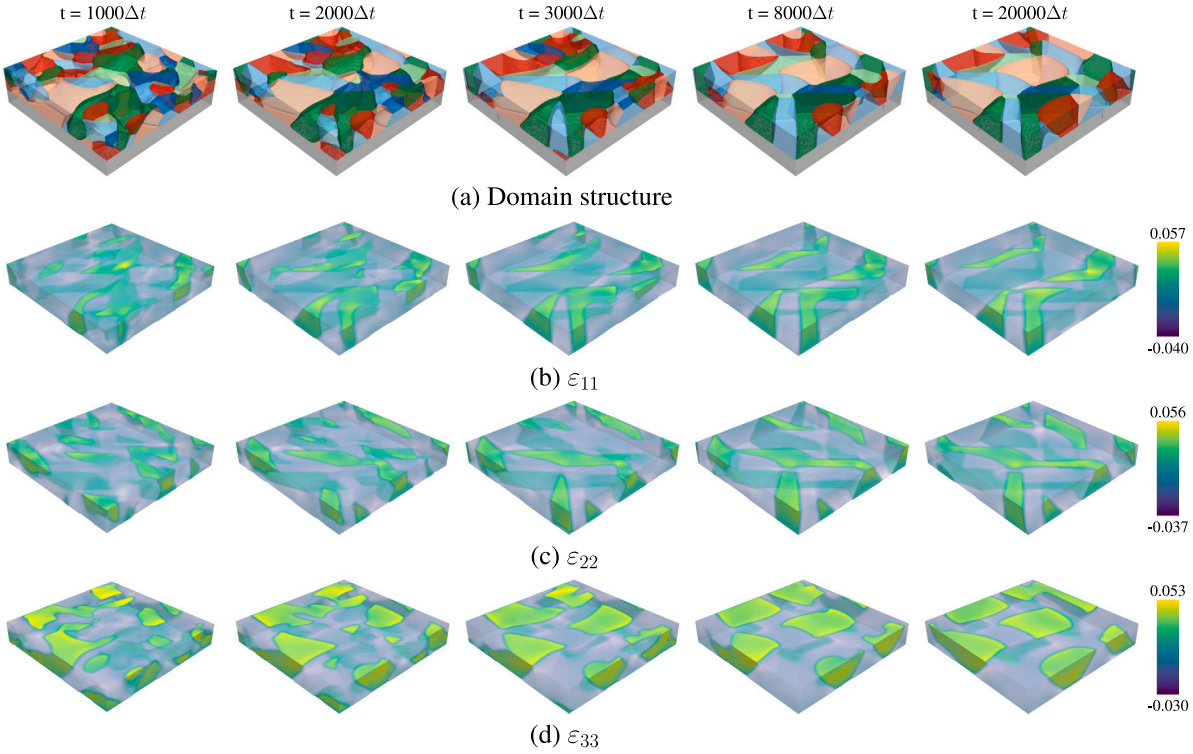

Fig. 6. The temporal evolution of domain structures, together with the corresponding ϵ_{11}, ϵ_{22}, and ϵ_{33}, at $\epsilon^{\text{mis}} = 0.006$.

The computed domain structures, the volume fraction of the c-domains, and the dimensional elastic energy with varying film thickness are shown in Fig. 8. In addition, the temporal evolution of domain formation and the associated strain distributions for three distinct film thicknesses, namely h_f = 10, 30, 50 nm, are shown in Figs. 9 to 11. It is shown that the morphology of the domains exhibits a discernible dependence on thickness. Another remarkable observation is the reduction of domains a_1 and a_2 with increased film thickness. This aligns with the trend depicted in the volume fraction plot of c-domains, which demonstrates an increase corresponding to larger film thicknesses. In

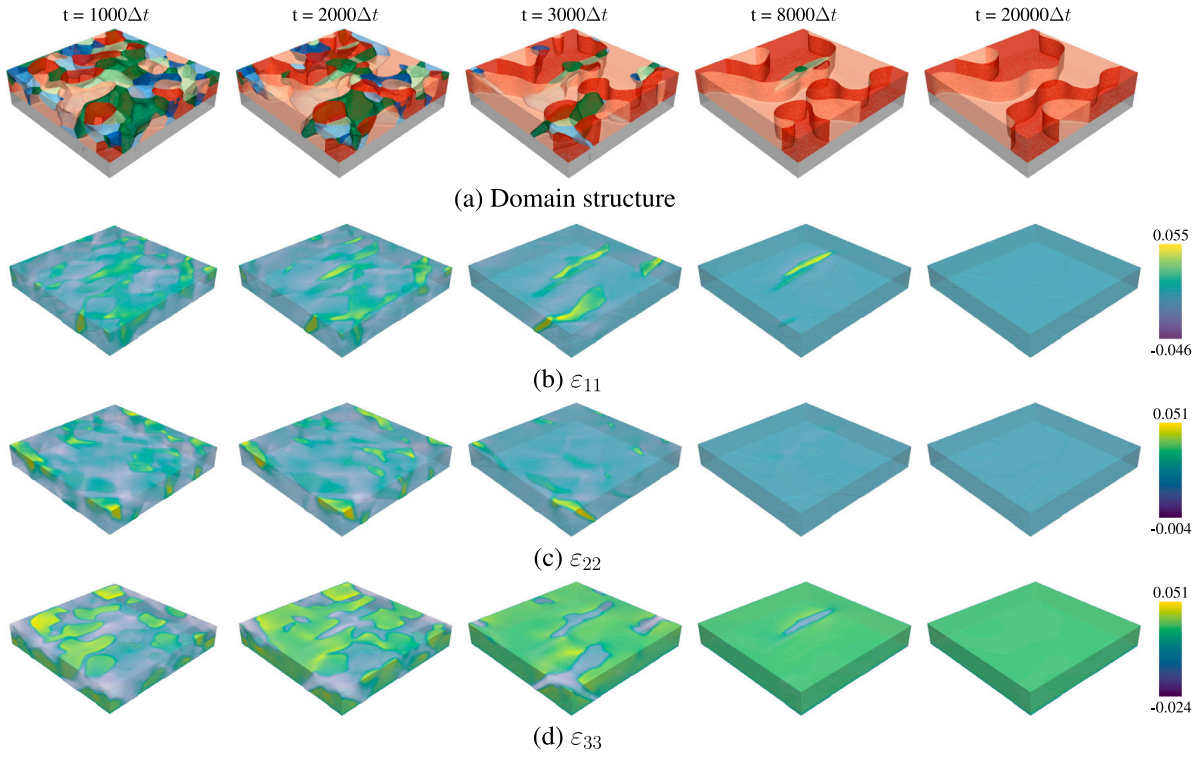

Fig. 7. The temporal evolution of domain structures, together with the corresponding ε_{11}, ε_{22}, and ε_{33}, at $\varepsilon^{mis} = -0.003$.

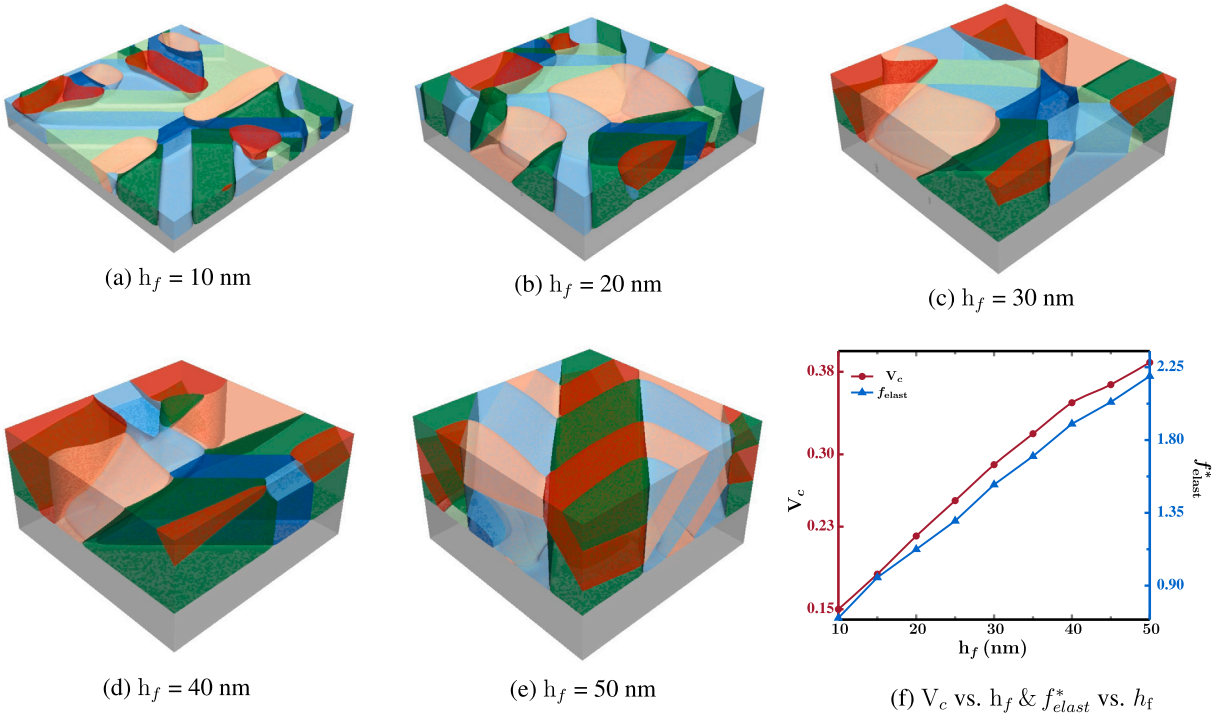

Fig. 8. Simulation result of (001)-oriented PTO with different thicknesses epitaxial thin films grown on KTO substrates. (a)–(e) represent the domain structures, while (f) shows the variations of the elastic energy f_{elast} as well as the volume fraction of the c-domain with varying film thickness.

addition, the computed increase in elastic energy with increasing film thickness also indicates that greater elastic energy contributes to the stability of the c-domains.

The temporal evolution of the film at different film thicknesses, denoted as h_f = 10, 30, 50 nm (Figs. 9–11), shows a decreasing trend in the distributions of ε_{11} and ε_{22}, alongside an increasing trend in the distribution of ε_{33}. This observed behavior correlates with the increase in c-domains with increasing film thickness. In particular, the significant increase in the c-domains is attributed to the phenomenon of strain relaxation in the system. Thicker films can be subjected to relatively less strain than their thinner counterparts. In thin films, strains due to substrate or lattice mismatches can have an influence on the domain

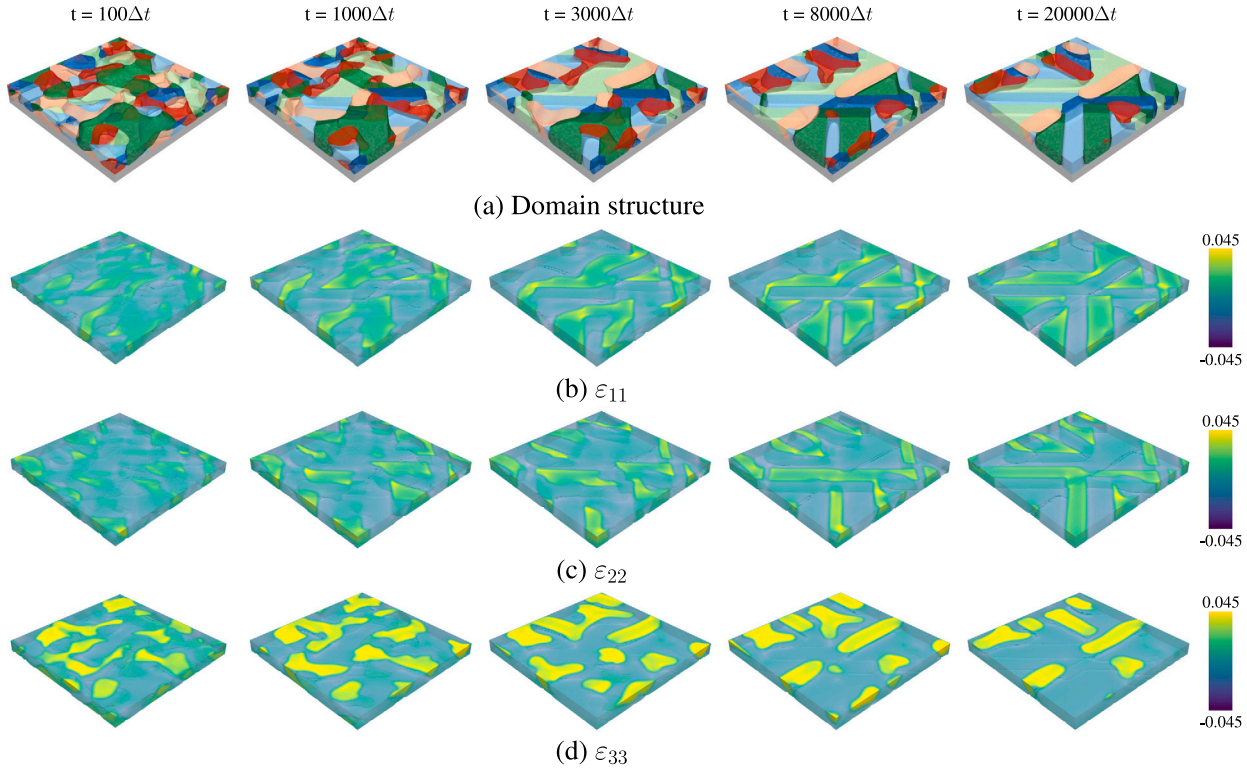

Fig. 9. The evolution of the domain morphology and strain distribution for a film thickness of $h_f = 10\,\text{nm}$, at various time steps.

structure. As film thickness increases, the formation and stability of c-domains are enhanced due to an increased tendency toward strain relaxation. It should be noted that although the observed phenomena of an increasing c-domain with higher film thickness are consistent with the results in Ref. [15], there is a discrepancy in the quantitative assessment of the c-domain between the present study and the above reference. This discrepancy could be attributed to the application of the short-circuited boundary condition, which has been demonstrated to promote the formation of c-domains, aligning with the aforementioned outcome. Consequently, this condition identifies a non-negligible volume fraction of the c-domain, even when the film thickness h_f is set to 10 nm. Furthermore, in this study, the material parameters of KTO were used as input for the simulations to replicate a real system, while the details corresponding to Ref. [15] are not clearly specified.

4.4. Temperature-dependent domain fraction and configuration

This study also investigates the growth of (001)-oriented PTO films with $128 \times 128 \times 40$ cells on KTO substrates under varying temperature conditions. Since the temperature influences the thermal expansion, the thermal vibrations, and the phase transitions [48], a temperature-dependent modulation of the spontaneous polarization and the inelastic strain is to be expected. The decrease in spontaneous polarization with an increasing temperature within the PTO material has been discussed in Ref. [49], which we have included as a key input for the current simulation. In view of the different thermal expansion properties of PTO and KTO, the temperature-dependent misfit strain in the PTO thin film and the KTO substrate is defined as follows:

$$\begin{aligned} \tilde{\varepsilon}_{ij}^{\text{mis},f} &= \tilde{\varepsilon}_{ij}^{0} + \alpha_f \Delta T \\ \tilde{\varepsilon}_{ij}^{\text{mis},s} &= \tilde{\varepsilon}_{ij}^{0} + \alpha_s \Delta T, \end{aligned} \tag{21}$$

in which $i, j = 1, 2$ and $\varepsilon_{12}^{\text{mis}} = 0$. Since the lattice distortion used to evaluate the electrostatic coefficients has a temperature-dependent trend analogous to that of spontaneous polarization, it can lead to unnoticed changes in the electrostatic coefficients, as also described in Ref. [49]. Consequently, the resulting electrostatic coefficients are considered to be independent of temperature, while the temperature-induced changes in the spontaneous strain within the PTO film are primarily attributed to variations in spontaneous polarization. α_f and α_s in Eq. (21) denote the thermal expansion coefficients for PTO and KTO, respectively, as given in Table 1. As discussed in the previous subsection, $\tilde{\varepsilon}_{ij}^{0} \approx 0.83\%$ characterizes the mismatch between PTO and KTO at room temperature. Moreover, ΔT denotes the temperature differential between the simulated temperature and the room temperature. In accordance with the formulae shown in Eq. (21), the graphical representation of the temperature-dependent misfit strains of the PTO and KTO systems, which do not consider the spontaneous strain, can be seen in Fig. 12(a).

The initial configuration for this simulation was taken from Fig. 4 and served as the basic reference. A homogeneous temperature distribution is considered for each simulation. The structural attributes of the domain at different temperature points were shown in Fig. 13, while the computed volume fraction of the c-domain and average elastic energy was explained in Fig. 12(b). The observation from Fig. 13 illustrates the temperature-dependent differences in the domain morphologies, with a noticeable decrease in the c-domain, as the temperature increases. As the temperature increases, the magnitude of misfit strain increases for both PTO and KTO materials. In light of the preceding subsection, we have inferred that the tensile misfit favors the formation of a-domains, thereby resulting in a reduction of c-domains at elevated temperatures. In addition, it becomes clear that the distinctive thermal expansion properties of PTO and KTO lead to different amplitudes of the increase of the eigenstrain (Fig. 12(a)). In turn, this phenomenon contributes to the sustained existence of c-domains, even at the elevated temperature of 400 °C, with a tensile misfit strain of 0.0125 in the PTO film. This observation diverges from the findings in the simulation results shown in Fig. 4, where it was noted that the stability of the c-domains could not be maintained under a tensile strain of 0.012.

The computed V_c in Fig. 12(b) (marked by the dark red line) shows a decrease with increasing temperature. This observation is consistent with the expected variation in domain morphology. Besides, the ob-

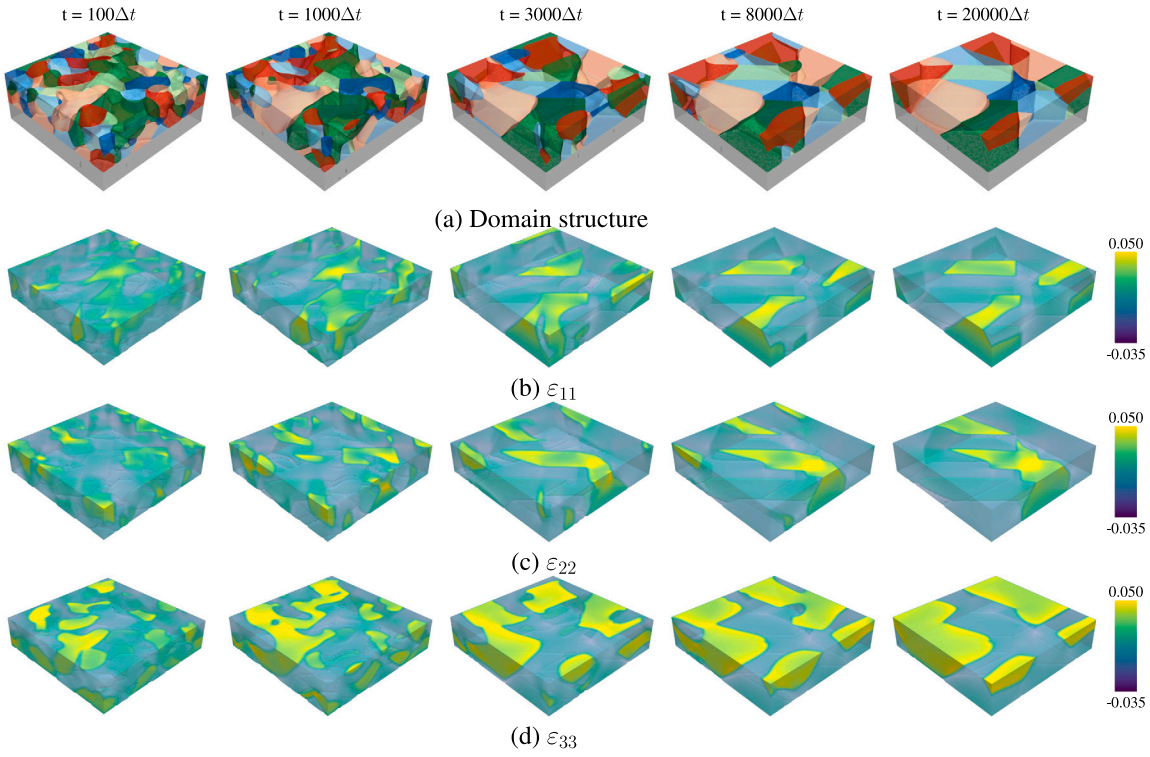

Fig. 10. The evolution of the domain morphology and strain distribution for a film thickness of $h_f = 30\,\text{nm}$, at different time steps.

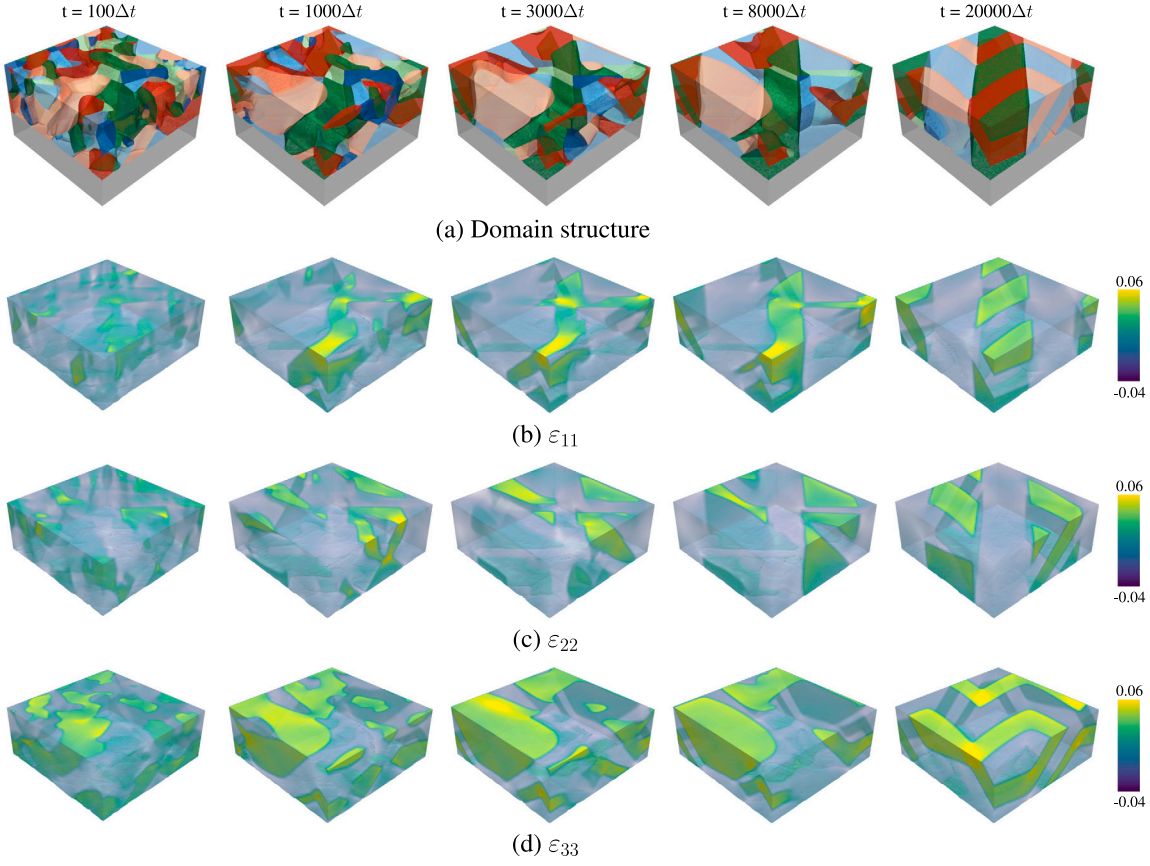

Fig. 11. The evolution of the domain morphology and strain distribution for a film thickness of $h_f = 50\,\text{nm}$, at different time steps.

served phenomenon of PTO growth on KTO, at varying temperatures, is also consistent with the findings in Ref. [50]. In Fig. 12(b), the variation of the average elastic energy density of the thin film with temperature is depicted by the dark blue line. It is evident that a

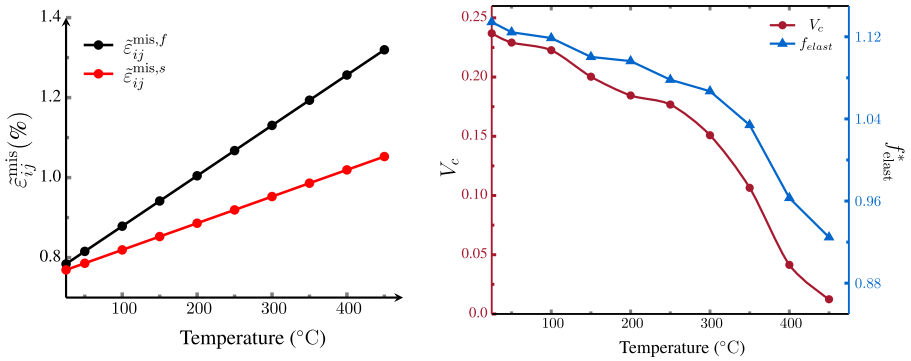

(a) ε_{ij}^{mis} vs. Temperature (b) V_{c} & f_{elast} vs. Temperature

Fig. 12. (a) represents the temperature-dependent elastic strain of the PTO and KTO systems without considering the spontaneous strain; (b) shows the change in the volume fraction of the c-domain (V_c) and the average elastic energy density (f^*_{elast}) with temperature.

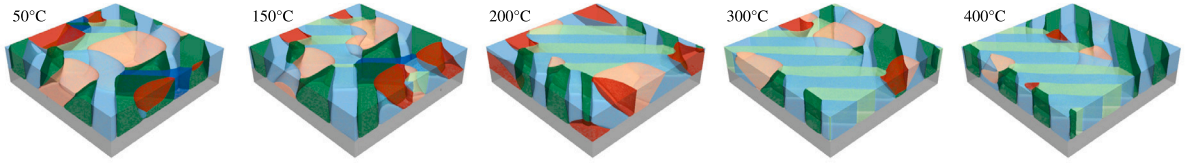

Fig. 13. Domain configuration of (001)-oriented PTO epitaxial thin films on KTO substrate, at different growth temperatures.

similar trend has been observed, where f_{elast} decreases with increasing temperature. The simulation results shown in Fig. 3 clearly indicate that a higher average elastic energy within the thin film system contributes significantly to maintaining the stability of the c-domain. As temperature increases, the growing magnitude of inelastic strain leads to a reduction in the elastic energy within the thin film. This reduction in elastic energy subsequently weakens the driving force responsible for the transformation from the a-domains to the c-domains. Consequently, at higher temperatures, the c-domains decrease and the system reaches an equilibrium with different domain structures, all driven by the minimization of the total energy. It is worth mentioning that the energy density f_{elec} also shows a decreasing tendency with increasing temperature. Nonetheless, given its relatively insignificant impact on the overall analysis, we have made a deliberate decision not to take it into account in this particular context. The temporal evolution of domain structure formation and associated changes in the three main strains for temperature at 25, 200 and 400 °Celsius are also documented in Appendix B. There is an obvious trend in which the distribution of ε_{33} shows a decreasing pattern associated with increasing temperatures. This phenomenon indicates a correlated reduction in elastic energy, with increasing temperature. Consequently, the observed decrease in the occurrence of c-domains is associated with increased temperatures.

Using the proposed model, we have successfully computed the domain structures for films grown on a cubic substrate, considering factors such as substrate deformation, misfit effects, film thickness, and temperature variations. Those simulated results align well with both theoretical predictions and experimental observations documented in the literature [12,15,50]. In addition, with our new model, we can analyze the reasons for domain structure formation under different conditions by examining and comparing the elastic and electric energies of the films.

5. Conclusion and outlook

In summary, our research has advanced the application of the multiphase-field approach to compute domain structures in ferroelectric thin films, building on the fundamental principles described in our previous work [29]. Specifically, we performed simulations using PTO as a model material, starting with an analysis of substrate deformation. Subsequently, the growth of PTO on different substrates was investigated under varying misfit strain conditions. In the final phase of our study, we extended our research to the growth of PTO on KTO, incorporating a range of temperatures and different film thickness. By replacing the Landau potential and gradient energy in the TDGL model with the interfacial energy in the multiphase-field framework, our model provides an effective alternative to characterize the ferroelectric phase transformation and domain wall properties. This comprehensive approach allowed us to gain insights into the different domain structure in variations ferroelectrics. For instance, this method opens up the possibility of using phase-field simulations to study a unique and emerging semiconductor ferroelectric, such as $MAPbI_3$.

CRediT authorship contribution statement

Ling Fan: Writing – review & editing, Writing – original draft, Visualization, Validation, Methodology, Investigation, Formal analysis, Conceptualization. **Martin Reder:** Writing – review & editing, Software. **Daniel Schneider:** Writing – review & editing, Conceptualization. **Manuel Hinterstein:** Writing – review & editing. **Britta Nestler:** Writing – review & editing, Supervision, Funding acquisition.

Declaration of competing interest

The authors declare that they have no known competing financial interests or personal relationships that could have appeared to influence the work reported in this paper.

Data availability

Data will be made available on request.

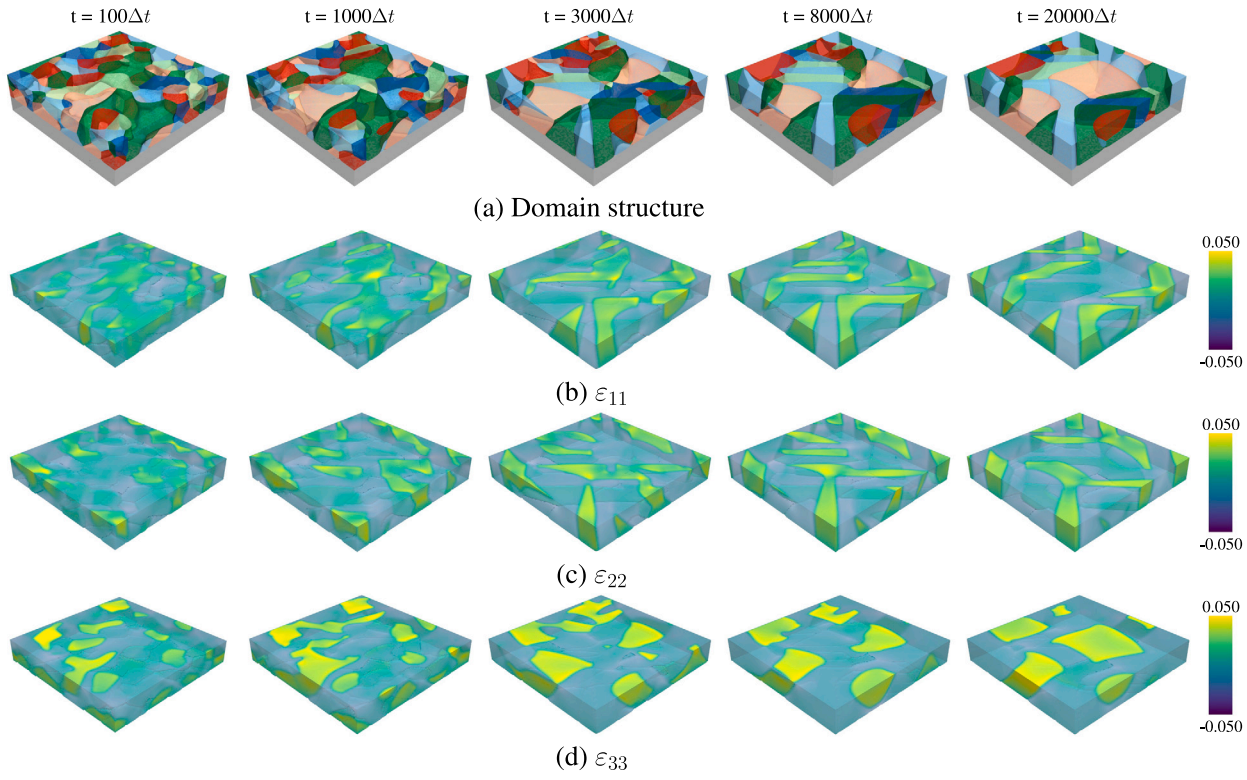

Fig. 14. The temporal evolution of the domain structures, together with the corresponding ε_{11}, ε_{22}, and ε_{33}, at 25 °C.

Acknowledgments

Ling Fan expresses gratitude for the financial support received from the China Scholarship Council and the KeraSolar project, funded by the Carl Zeiss Foundation. Daniel Schneider and Britta Nestler acknowledge funding through the Helmholtz association within programmer MSE, Germany, no. 43.31.01. Manuel Hinterstein thanks the Fraunhofer Internal Programs, Germany (grant no. Attract 40-04857) for financial support. The authors would like to thank the state of Baden-Württemberg for support within the bwHPC program. Lastly, the authors express their gratitude toward Leon Geisen for his contribution to improving the English language of this manuscript.

Appendix A. A brief introduction of the jump condition approach

Using the equilibrium jump condition, which establishes a force balance along the normal vector of the interface and adheres to the Hadamard condition in the tangential direction [30,35], the primary objective is to transform stresses and strains into a reference frame that is aligned with the interface orientation. Subsequently, energy can be calculated using locally averaged variables. To achieve this objective, a scalar field $L(\boldsymbol{\phi}) = \sum_{\alpha<\beta} \phi_\alpha \phi_\beta$ is introduced and a homogenized normal vector $\boldsymbol{n}$, which effectively accounts for the influence of the interface orientation, can be defined as:

$$\boldsymbol{n} = \frac{\nabla L(\boldsymbol{\phi})}{|\nabla L(\boldsymbol{\phi})|}. \tag{22}$$

The stresses $\boldsymbol{\sigma}$ and strains $\boldsymbol{\epsilon}$ can then be transferred to a base $\boldsymbol{B}$, which is oriented by the unit vector $\boldsymbol{n}$. $\boldsymbol{B}$ is defined as $\boldsymbol{B} = (\boldsymbol{n}, \boldsymbol{t}, \boldsymbol{s})$, so that the orthogonality conditions $\boldsymbol{n}\cdot\boldsymbol{t} = \boldsymbol{n}\cdot\boldsymbol{s} = \boldsymbol{t}\cdot\boldsymbol{s} = 0$ are satisfied. In accordance with the force equilibrium condition, given as $[\![\boldsymbol{\sigma}_n]\!] = \boldsymbol{0}$, and the kinematic Hadamard compatibility condition, expressed as $[\![\boldsymbol{\epsilon}_t]\!] = \boldsymbol{0}$, for an infinitesimal deformation in a singular plane, the stresses and strains can be expressed as follows, using the Voigt notation:

$$\begin{aligned}
\boldsymbol{\sigma}^\alpha_{\boldsymbol{B}}(\boldsymbol{n}) &:= \left(\sigma_{nn}, \sigma_{nt}, \sigma_{ns}, \sigma_{tt}, \sigma_{ss}\, \sigma_{ts}\right)^{\mathrm{T}} = (\boldsymbol{\sigma}_n, \boldsymbol{\sigma}^\alpha_t)^{\mathrm{T}}, \\
\boldsymbol{\epsilon}^\alpha_{\boldsymbol{B}}(\boldsymbol{n}) &:= \left(\varepsilon_{nn}, 2\varepsilon_{nt}, 2\varepsilon_{ns}, \varepsilon_{tt}, 2\varepsilon_{ss}\, \varepsilon_{ts}\right)^{\mathrm{T}} = (\boldsymbol{\epsilon}^\alpha_n, \boldsymbol{\epsilon}_t)^{\mathrm{T}}.
\end{aligned} \tag{23}$$

Here, the order is interchanged to distinguish the continuous contribution ($\boldsymbol{\sigma}_{\boldsymbol{n}} := (\sigma_{nn}, \sigma_{nt}, \sigma_{ns})^{\mathrm{T}}$, $\boldsymbol{\epsilon}_t := (\varepsilon_{tt}, 2\varepsilon_{ss}\, \varepsilon_{ts})^{\mathrm{T}}$) and the discontinuous contribution ($\boldsymbol{\sigma}^\alpha_t := (\sigma_{tt}, \sigma_{ss}\, \sigma_{ts})^{\mathrm{T}}$, $\boldsymbol{\epsilon}^\alpha_n := (\varepsilon_{nn}, 2\varepsilon_{nt}, 2\varepsilon_{ns})^{\mathrm{T}}$) [34]. Similarly, the stiffness tensor $\boldsymbol{C}^\alpha$ in the $\boldsymbol{B}$ base can be expressed as $\boldsymbol{C}^\alpha_{\boldsymbol{B}}$ and represented by the Voigt notation as follows:

$$\boldsymbol{C}^\alpha_{\boldsymbol{B}} := \begin{bmatrix} \boldsymbol{C}^\alpha_{nn} & \boldsymbol{C}^\alpha_{nt} \\ \boldsymbol{C}^\alpha_{tn} & \boldsymbol{C}^\alpha_{tt} \end{bmatrix} = \left[\begin{array}{ccc|ccc} C^\alpha_{nnnn} & C^\alpha_{nnnt} & C^\alpha_{nnns} & C^\alpha_{nntt} & C^\alpha_{nnss} & C^\alpha_{nnts} \\ C^\alpha_{ntnn} & C^\alpha_{ntnt} & C^\alpha_{ntns} & C^\alpha_{nttt} & C^\alpha_{ntss} & C^\alpha_{ntts} \\ C^\alpha_{nsnn} & C^\alpha_{nsnt} & C^\alpha_{nsns} & C^\alpha_{nstt} & C^\alpha_{nsss} & C^\alpha_{nsts} \\ \hline C^\alpha_{ttnn} & C^\alpha_{ttnt} & C^\alpha_{ttns} & C^\alpha_{tttt} & C^\alpha_{ttss} & C^\alpha_{ttts} \\ C^\alpha_{ssnn} & C^\alpha_{ssnt} & C^\alpha_{ssns} & C^\alpha_{sstt} & C^\alpha_{ssss} & C^\alpha_{ssts} \\ C^\alpha_{tsnn} & C^\alpha_{tsnt} & C^\alpha_{tsns} & C^\alpha_{tstt} & C^\alpha_{tsss} & C^\alpha_{tsts} \end{array}\right]. \tag{24}$$

In this context, $\boldsymbol{C}^\alpha_{nn}$ and $\boldsymbol{C}^\alpha_{tt}$ are symmetric 3×3 matrices, while $\boldsymbol{C}^\alpha_{nt}$ and $\boldsymbol{C}^\alpha_{tn}$ are 3×3 matrices that satisfy the required condition $\boldsymbol{C}^\alpha_{nt} = [\boldsymbol{C}^\alpha_{tn}]^{\mathrm{T}}$. With the established notations, the strain energy density associated

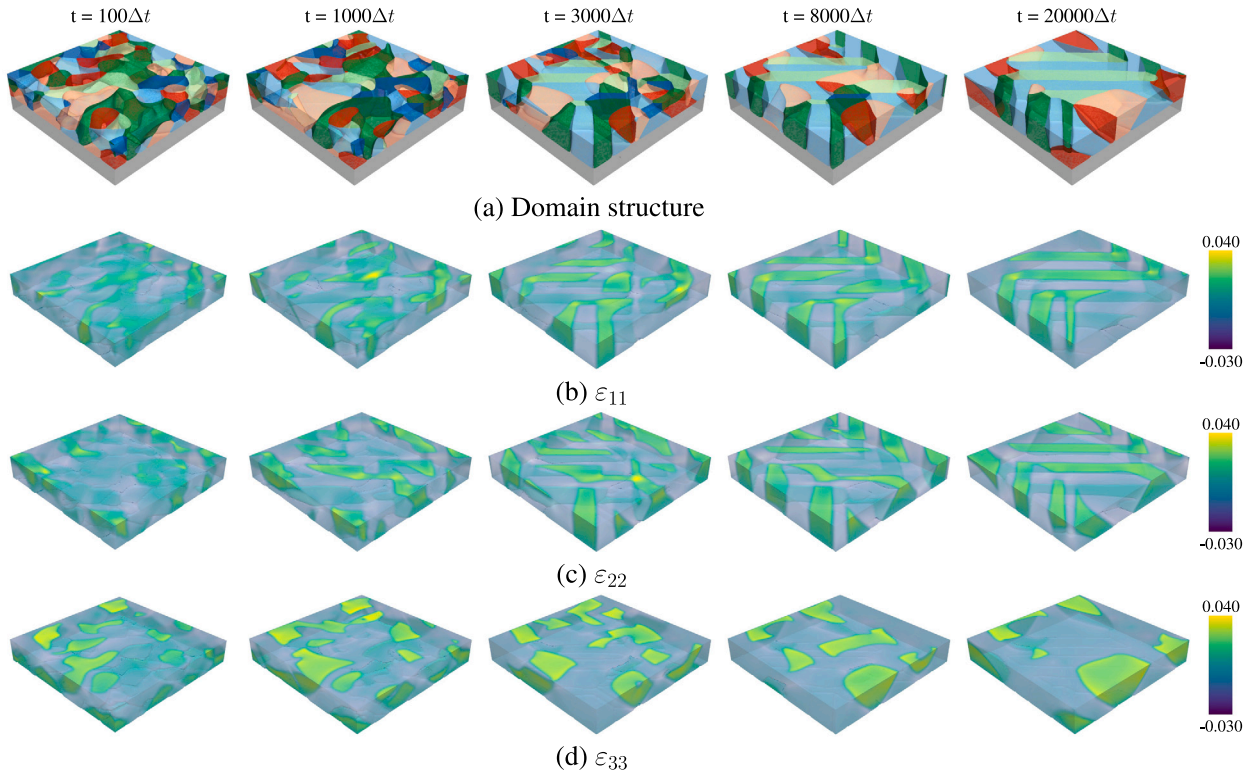

Fig. 15. The temporal evolution of the domain structures, together with the corresponding ε_{11}, ε_{22}, and ε_{33}, at 200 °C.

with phase α can be expressed as:

$$f^{\alpha}(\boldsymbol{\varepsilon}_{\boldsymbol{B}}^{\alpha}) = \frac{1}{2}\left[(\boldsymbol{\varepsilon}_{n}^{\alpha} - \tilde{\boldsymbol{\varepsilon}}_{n}^{\alpha}) \cdot \boldsymbol{C}_{nn}^{\alpha}(\boldsymbol{\varepsilon}_{n}^{\alpha} - \tilde{\boldsymbol{\varepsilon}}_{n}^{\alpha}) + (\boldsymbol{\varepsilon}_{n}^{\alpha} - \tilde{\boldsymbol{\varepsilon}}_{n}^{\alpha}) \cdot \boldsymbol{C}_{nt}^{\alpha}(\boldsymbol{\varepsilon}_{t}^{\alpha} - \tilde{\boldsymbol{\varepsilon}}_{t}^{\alpha}) + (\boldsymbol{\varepsilon}_{t}^{\alpha} - \tilde{\boldsymbol{\varepsilon}}_{t}^{\alpha}) \cdot \boldsymbol{C}_{tn}^{\alpha}(\boldsymbol{\varepsilon}_{n}^{\alpha} - \tilde{\boldsymbol{\varepsilon}}_{n}^{\alpha}) + (\boldsymbol{\varepsilon}_{t}^{\alpha} - \tilde{\boldsymbol{\varepsilon}}_{t}^{\alpha}) \cdot \boldsymbol{C}_{tt}^{\alpha}(\boldsymbol{\varepsilon}_{t}^{\alpha} - \tilde{\boldsymbol{\varepsilon}}_{t}^{\alpha})\right] \tag{25}$$

Therefore, the strain energy density in a multiphase framework is determined by the linear interpolation of the individual contributions, using the interpolation function $h^{\alpha}(\boldsymbol{\phi})$, which is written as follows:

$$\bar{f}(\boldsymbol{\phi}, \boldsymbol{\varepsilon}_{\boldsymbol{B}}) = \sum_{\alpha} f^{\alpha}(\boldsymbol{\varepsilon}_{\boldsymbol{B}}^{\alpha}) h^{\alpha}(\boldsymbol{\phi}). \tag{26}$$

The treatment of the variation derivative for this strain energy will be addressed subsequently.

The overall elastic potential $W(\boldsymbol{\phi}, \boldsymbol{\sigma}_n, \boldsymbol{\varepsilon}_t)$ is defined as:

$$W(\boldsymbol{\varepsilon}_t, \boldsymbol{\sigma}_n, \boldsymbol{\phi}) = \sum_{\alpha}\left[\begin{pmatrix}\boldsymbol{\sigma}_n \\ \boldsymbol{\varepsilon}_t\end{pmatrix} \cdot \tilde{\boldsymbol{\mathcal{T}}}^{\alpha} \begin{pmatrix}\boldsymbol{\sigma}_n \\ \boldsymbol{\varepsilon}_t\end{pmatrix} - \begin{pmatrix}\boldsymbol{\sigma}_n \\ \boldsymbol{\varepsilon}_t\end{pmatrix} \cdot \begin{pmatrix}\boldsymbol{I} & \boldsymbol{\mathcal{T}}_{nt}^{\alpha} \\ \boldsymbol{0} & \boldsymbol{\mathcal{T}}_{tt}^{\alpha}\end{pmatrix} \begin{pmatrix}\tilde{\boldsymbol{\varepsilon}}_n^{\alpha} \\ \tilde{\boldsymbol{\varepsilon}}_t^{\alpha}\end{pmatrix} + \frac{1}{2}\left(\tilde{\boldsymbol{\varepsilon}}_t^{\alpha} \cdot \boldsymbol{\mathcal{T}}_{tt}^{\alpha} \tilde{\boldsymbol{\varepsilon}}_t^{\alpha}\right)\right] h^{\alpha}(\boldsymbol{\phi}). \tag{27}$$

In Eq. (27), $\boldsymbol{I}$ and $\boldsymbol{0}$ are the second-order identity and zero tensors, respectively. $\tilde{\boldsymbol{\mathcal{T}}}^{\alpha}$ is a proportionality matrix, introduced as:

$$\tilde{\boldsymbol{\mathcal{T}}}^{\alpha} = \begin{pmatrix}\tilde{\boldsymbol{\mathcal{T}}}_{nn}^{\alpha} & \tilde{\boldsymbol{\mathcal{T}}}_{nt}^{\alpha} \\ \tilde{\boldsymbol{\mathcal{T}}}_{tn}^{\alpha} & \tilde{\boldsymbol{\mathcal{T}}}_{tt}^{\alpha}\end{pmatrix}, \tag{28}$$

where each element of $\tilde{\boldsymbol{\mathcal{T}}}^{\alpha}$ corresponds to an interpolated block and reads:

$$\begin{aligned} \boldsymbol{\mathcal{T}}_{nn}^{\alpha} &:= -(\boldsymbol{C}_{nn}^{\alpha})^{-1} \\ \boldsymbol{\mathcal{T}}_{nt}^{\alpha} &:= -(\boldsymbol{C}_{nn}^{\alpha})^{-1}\boldsymbol{C}_{nt}^{\alpha} \\ \boldsymbol{\mathcal{T}}_{tt}^{\alpha} &:= -\left(\boldsymbol{C}_{tt}^{\alpha} - \boldsymbol{C}_{tn}^{\alpha}(\boldsymbol{C}_{nn}^{\alpha})^{-1}\boldsymbol{C}_{nt}^{\alpha}\right). \end{aligned} \tag{29}$$

On the basis of Ref. [34], the stress $\bar{\boldsymbol{\sigma}}_B$ can be derived from the potential $W(\boldsymbol{\sigma}_n, \boldsymbol{\varepsilon}_t, \boldsymbol{\phi})$ in a multiphase system, which can be written as:

$$\bar{\boldsymbol{\sigma}}_B = \begin{bmatrix} -[\tilde{\boldsymbol{\mathcal{T}}}_{nn}]^{-1} & -[\tilde{\boldsymbol{\mathcal{T}}}_{nn}]^{-1}\tilde{\boldsymbol{\mathcal{T}}}_{nt} \\ -\tilde{\boldsymbol{\mathcal{T}}}_{tn}[\tilde{\boldsymbol{\mathcal{T}}}_{nn}]^{-1} & \tilde{\boldsymbol{\mathcal{T}}}_{tt} - \tilde{\boldsymbol{\mathcal{T}}}_{tn}[\tilde{\boldsymbol{\mathcal{T}}}_{nn}]^{-1}\tilde{\boldsymbol{\mathcal{T}}}_{nt} \end{bmatrix} \begin{bmatrix} \boldsymbol{\varepsilon}_n \\ \boldsymbol{\varepsilon}_t \end{bmatrix} + \begin{bmatrix} [\tilde{\boldsymbol{\mathcal{T}}}_{nn}]^{-1} & \boldsymbol{0} \\ \tilde{\boldsymbol{\mathcal{T}}}_{tn}[\tilde{\boldsymbol{\mathcal{T}}}_{nn}]^{-1} & -\boldsymbol{I} \end{bmatrix} \begin{bmatrix} \tilde{\boldsymbol{\mathcal{X}}}_n \\ \tilde{\boldsymbol{\mathcal{X}}}_t \end{bmatrix}. \tag{30}$$

The components of the averaged proportionality matrix $\tilde{\boldsymbol{\mathcal{T}}}$ in Eq. (30) are determined by $\tilde{\boldsymbol{\mathcal{T}}}_{ij} = \sum_{\alpha} \tilde{\boldsymbol{\mathcal{T}}}_{ij}^{\alpha} h^{\alpha}(\boldsymbol{\phi})$. $\tilde{\boldsymbol{\mathcal{X}}}_n$ and $\tilde{\boldsymbol{\mathcal{X}}}_t$ are the respective normal and tangential components of the interpolated nonelastic strain, which can be defined as follows:

$$\begin{aligned} \tilde{\boldsymbol{\mathcal{X}}}_n &= \sum_{\alpha}\left[\tilde{\boldsymbol{\varepsilon}}_n^{\alpha} + \boldsymbol{\mathcal{T}}_{nt}^{\alpha}\tilde{\boldsymbol{\varepsilon}}_t^{\alpha}\right] h^{\alpha}(\boldsymbol{\phi}) \\ \tilde{\boldsymbol{\mathcal{X}}}_t &= \sum_{\alpha} \boldsymbol{\mathcal{T}}_{tt}^{\alpha}\tilde{\boldsymbol{\varepsilon}}_t^{\alpha} h^{\alpha}(\boldsymbol{\phi}). \end{aligned} \tag{31}$$

Appendix B. Simulations of PTO growth on KTO, at different temperatures

See Figs. 14–16.

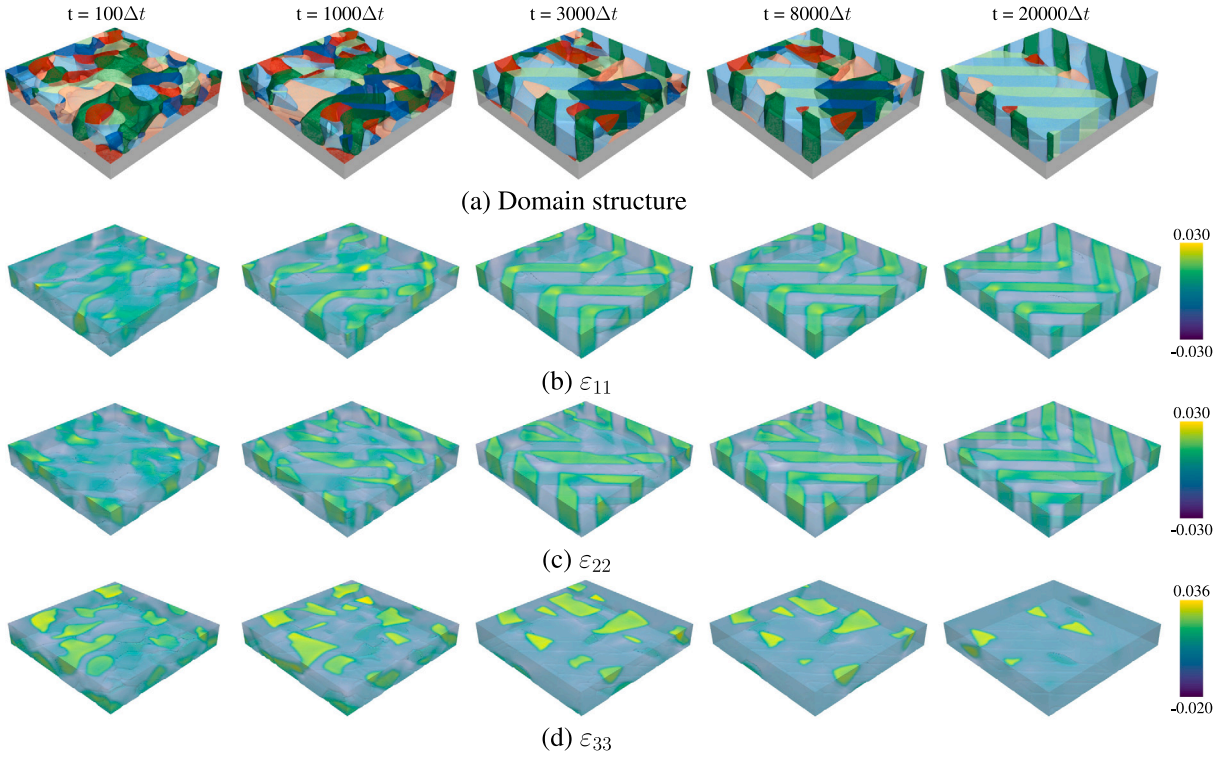

Fig. 16. The temporal evolution of the domain structures, together with the corresponding ϵ_{11}, ϵ_{22}, and ϵ_{33}, at 400 °C.

References

[1] P. Muralt, Ferroelectric thin films for micro-sensors and actuators: a review, J. Micromech. Microeng. 10 (2) (2000) 136.

[2] N. Setter, D. Damjanovic, L. Eng, G. Fox, S. Gevorgian, S. Hong, A. Kingon, H. Kohlstedt, N. Park, G. Stephenson, et al., Ferroelectric thin films: Review of materials, properties, and applications, J. Appl. Phys. 100 (5) (2006).

[3] L. You, F. Zheng, L. Fang, Y. Zhou, L. Tan, Z. Zhang, G. Ma, D. Schmidt, A. Rusydi, L. Wang, et al., Enhancing ferroelectric photovoltaic effect by polar order engineering, Sci. Adv. 4 (7) (2018) eaat3438.

[4] A. Fernandez, M. Acharya, H. Lee, J. Schimpf, Y. Jiang, D. Lou, Z. Tian, L. Martin, Thin-film ferroelectrics, Adv. Mater. 34 (30) (2022) 2108841.

[5] W. Cao, L. Cross, Theory of tetragonal twin structures in ferroelectric perovskites with a first-order phase transition, Phys. Rev. B 44 (1) (1991) 5.

[6] S. Nambu, D. Sagala, Domain formation and elastic long-range interaction in ferroelectric perovskites, Phys. Rev. B 50 (9) (1994) 5838.

[7] H. Hu, L. Chen, Three-dimensional computer simulation of ferroelectric domain formation, J. Am. Ceram. Soc. 81 (3) (1998) 492–500.

[8] Y. Li, S. Hu, Z. Liu, L. Chen, Effect of electrical boundary conditions on ferroelectric domain structures in thin films, Appl. Phys. Lett. 81 (3) (2002) 427–429.

[9] J. Wang, S. Shi, L. Chen, Y. Li, T. Zhang, Phase-field simulations of ferroelectric/ferroelastic polarization switching, Acta Mater. 52 (3) (2004) 749–764.

[10] L. Chen, Phase-field method of phase transitions/domain structures in ferroelectric thin films: a review, J. Am. Ceram. Soc. 91 (6) (2008) 1835–1844.

[11] J. Wang, B. Wang, L. Chen, Understanding, predicting, and designing ferroelectric domain structures and switching guided by the phase-field method, Annu. Rev. Mater. Res. 49 (2019) 127–152.

[12] Y. Li, S. Hu, Z. Liu, L. Chen, Effect of substrate constraint on the stability and evolution of ferroelectric domain structures in thin films, Acta Mater. 50 (2) (2002) 395–411.

[13] Y. Li, L. Chen, Temperature-strain phase diagram for $BaTiO_3$ thin films, Appl. Phys. Lett. 88 (7) (2006).

[14] D. Schlom, L. Chen, C. Eom, K. Rabe, S. Streiffer, J. Triscone, Strain tuning of ferroelectric thin films, Annu. Rev. Mater. Res. 37 (2007) 589–626.

[15] G. Sheng, J. Hu, J. Zhang, Y. Li, Z. Liu, L. Chen, Phase-field simulations of thickness-dependent domain stability in $PbTiO_3$ thin films, Acta Mater. 60 (8) (2012) 3296–3301.

[16] D. Liu, J. Wang, H. Jafri, X. Wang, X. Shi, D. Liang, C. Yang, X. Cheng, H. Huang, Phase-field simulations of vortex chirality manipulation in ferroelectric thin films, npj QM. 7 (1) (2022) 34.

[17] H. Chen, A. Soh, Y. Ni, Phase field modeling of flexoelectric effects in ferroelectric epitaxial thin films, Acta Mech. 225 (4–5) (2014) 1323–1333.

[18] D. Liu, X. Shi, J. Wang, X. Cheng, H. Huang, Phase-field simulations of surface charge-induced ferroelectric vortex, J. Phys. D: Appl. Phys. 54 (40) (2021) 405302.

[19] J. Wang, T. Yang, J. Zorn, E. Wang, J. Irwin, S. Lindemann, M. Rzchowski, J. Hu, C. Eom, L. Chen, Strain anisotropy and magnetic domain structures in multiferroic heterostructures: High-throughput finite-element and phase-field studies, Acta Mater. 176 (2019) 73–83.

[20] W. Chen, Y. Zheng, Vortex switching in ferroelectric nanodots and its feasibility by a homogeneous electric field: effects of substrate, dislocations and local clamping force, Acta Mater. 88 (2015) 41–54.

[21] Y. Ji, W. Chen, Y. Zheng, Crossover of polar and toroidal orders in ferroelectric nanodots with a morphotropic phase boundary and nonvolatile polar-vortex transformations, Phys. Rev. B 100 (1) (2019) 014101.

[22] J. Wang, M. Kamlah, T. Zhang, Y. Li, L. Chen, Size-dependent polarization distribution in ferroelectric nanostructures: Phase field simulations, Appl. Phys. Lett. 92 (16) (2008) 162905.

[23] J. Liu, Y. Ji, S. Yuan, L. Ding, W. Chen, Y. Zheng, Controlling polar-toroidal multi-order states in twisted ferroelectric nanowires, Npj Comput. Mater. 4 (1) (2018) 78.

[24] Q. Li, C. Nelson, S. Hsu, A. Damodaran, L. Li, A. Yadav, M. McCarter, L. Martin, R. Ramesh, S. Kalinin, Quantification of flexoelectricity in $PbTi_O3/SrTi_O3$ superlattice polar vortices using machine learning and phase-field modeling, Nature Commun. 8 (1) (2017) 1468.

[25] Y. Ji, W. Chen, Y. Zheng, The emergence of tunable negative electrocaloric effect in ferroelectric/paraelectric superlattices, J. Phys. D Appl. Phys. 53 (50) (2020) 505302.

[26] J. Wang, L. Chen, Strain control of domain structures in ferroelectric thin films: Applications of phase-field method, Handb. Mater. Model. Appl. (2020) 1213–1230.

[27] H. Röhm, T. Leonhard, M. Hoffmann, A. Colsmann, Ferroelectric poling of methylammonium lead iodide thin films, Adv. Funct. Mater. 30 (5) (2020) 1908657.

[28] H. Röhm, T. Leonhard, A. Schulz, S. Wagner, M. Hoffmann, A. Colsmann, Ferroelectric properties of perovskite thin films and their implications for solar energy conversion, Adv. Mater. 31 (26) (2019) 1806661.

[29] L. Fan, M. Reder, D. Schneider, M. Hinterstein, B. Nestler, A phase-field model for ferroelectric materials—Based on the multiphase-field method, Comput. Mater. Sci. 230 (2023) 112510.

[30] D. Schneider, S. Schmid, M. Selzer, T. Böhlke, B. Nestler, Small strain elasto-plastic multiphase-field model, Comput. Mech. 55 (1) (2015) 27–35.

[31] E. Schoof, D. Schneider, N. Streichhan, T. Mittnacht, M. Selzer, B. Nestler, Multiphase-field modeling of martensitic phase transformation in a dual-phase microstructure, Int. J. Solids Struct. 134 (2018) 181–194.
[32] B. Nestler, H. Garcke, B. Stinner, Multicomponent alloy solidification: phase-field modeling and simulations, Phys. Rev. E 71 (4) (2005) 041609.
[33] I. Steinbach, F. Pezzolla, A generalized field method for multiphase transformations using interface fields, Phys. D 134 (4) (1999) 385–393.
[34] D. Schneider, O. Tschukin, A. Choudhury, M. Selzer, T. Böhlke, B. Nestler, Phase-field elasticity model based on mechanical jump conditions, Comput. Mech. 55 (5) (2015) 887–901.
[35] D. Schneider, E. Schoof, O. Tschukin, A. Reiter, C. Herrmann, F. Schwab, M. Selzer, B. Nestler, Small strain multiphase-field model accounting for configurational forces and mechanical jump conditions, Comput. Mech. 61 (3) (2018) 277–295.
[36] C. Mennerich, F. Wendler, M. Jainta, B. Nestler, A phase-field model for the magnetic shape memory effect, Arch. Mech. 63 (5–6) (2011) 549–571.
[37] C. Mennerich, F. Wendler, M. Jainta, B. Nestler, Rearrangement of martensitic variants in Ni_2MnGa studied with the phase-field method, Eur. Phys. J. B. 86 (4) (2013) 1–9.
[38] D. Schneider, F. Schwab, E. Schoof, A. Reiter, C. Herrmann, M. Selzer, T. Böhlke, B. Nestler, On the stress calculation within phase-field approaches: a model for finite deformations, Comput. Mech. 60 (2) (2017) 203–217.
[39] Y. Zhang, F. Xue, Z. Chen, J. Liu, L. Chen, Presence of a purely tetragonal phase in ultrathin $BiFeO_3$ films: Thermodynamics and phase-field simulations, Acta Mater. 183 (2020) 110–117.
[40] I. Steinbach, Phase-field models in materials science, Modelling Simul. Mater. Sci. Eng. 17 (7) (2009) 073001.
[41] J. Hötzer, A. Reiter, H. Hierl, P. Steinmetz, M. Selzer, B. Nestler, The parallel multi-physics phase-field framework Pace3D, J. Comput. Sci. 26 (2018) 1–12.
[42] S. Choudhury, Y. Li, C. Krill III, L. Chen, Phase-field simulation of polarization switching and domain evolution in ferroelectric polycrystals, Acta Mater. 53 (20) (2005) 5313–5321.
[43] Y. Xu, S. Wu, L. Zhang, L. Wu, C. Ding, First-principles study of structural, electronic, elastic, and optical properties of cubic $KNbO_3$ and $KTaO_3$ crystals, Phys. Status Solidi. B 254 (5) (2017) 1600620.
[44] K. Lee, J. Choi, J. Lee, S. Baik, Domain formation in epitaxial $Pb(Zr_{1-x}Ti_x)O_3$ thin films, J. Appl. Phys. 90 (8) (2001) 4095–4102.
[45] Q. Qiu, V. Nagarajan, S. Alpay, Film thickness versus misfit strain phase diagrams for epitaxial $PbTiO_3$ ultrathin ferroelectric films, Phys. Rev. B 78 (6) (2008) 064117.
[46] R. People, J. Bean, Calculation of critical layer thickness versus lattice mismatch for Ge_xSi_{1-x}/Si strained-layer heterostructures, Appl. Phys. Lett. 47 (3) (1985) 322–324.
[47] R. People, J. Bean, Erratum: Calculation of critical layer thickness versus lattice mismatch for Ge_xSi_{1-x}/Si strained-layer heterostructures [Appl. Phys. Lett. 4 7, 322 (1985)], Appl. Phys. Lett. 49 (4) (1986) 229.
[48] A. Prahs, M. Reder, D. Schneider, B. Nestler, Thermomechanically coupled theory in the context of the multiphase-field method, Int. J. Mech. Sci. 257 (2023) 108484.
[49] M. Haun, E. Furman, S. Jang, H. McKinstry, L. Cross, Thermodynamic theory of $PbTiO_3$, J. Appl. Phys. 62 (8) (1987) 3331–3338.
[50] B. Kwak, A. Erbil, J. Budai, M. Chisholm, L. Boatner, B. Wilkens, Domain formation and strain relaxation in epitaxial ferroelectric heterostructures, Phys. Rev. B 49 (21) (1994) 14865.